

Surveys in Geophysics

May 2014, Volume 35, Issue 3, Pages 681-722

<http://dx.doi.org/10.1007/s10712-013-9244-0>

© Springer Science+Business Media Dordrecht 2013

Archimer
<http://archimer.ifremer.fr>

The original publication is available at <http://www.springerlink.com>

Sea Surface Salinity Observations from Space with the SMOS Satellite: A New Means to Monitor the Marine Branch of the Water Cycle

Nicolas Reul^{*,1,2}, Severine Fournier¹, Jaqueline Boutin³, Olga Hernandez³, Christophe Maes⁵,
Bertrand Chapron¹, Gaël Alory⁵, Yves Quilfen¹, Joseph Tenerelli⁴, Simmon Morisset³,
Yann Kerr⁶, Susanne Mecklenburg⁷, Steven Delwart⁷

¹ Laboratoire d'Océanographie Spatiale, Institut Français de recherche et d'Exploitation de la Mer, Centre Bretagne BP 70, 29280, Plouzané, France

² Centre Méditerranée, Zone Portuaire de Brégaillon, BP 330, 83507, La Seyne-sur-Mer Cedex, France

³ Laboratoire d'Océanographie et du Climat: Expérimentation et Approches Numériques, UMR 7159 CNRS/UPMC/IRD/MNH, Paris, France

⁵ LEGOS, OMP, CNAP, Université de Toulouse, Toulouse, France

⁴ CLS-Radar Division, Bâtiment Le Ponant, Avenue La Pérouse, Technopôle Brest-Iroise, 29280, Plouzané, France

⁶ CESBIO, Toulouse, France

⁷ ESA-ESRIN, Frascati, Italy

*: Corresponding author : Nicolas Reul, email address : nreul@ifremer.fr

Abstract:

While it is well known that the ocean is one of the most important component of the climate system, with a heat capacity 1,100 times greater than the atmosphere, the ocean is also the primary reservoir for freshwater transport to the atmosphere and largest component of the global water cycle. Two new satellite sensors, the ESA Soil Moisture and Ocean Salinity (SMOS) and the NASA Aquarius SAC-D missions, are now providing the first spaceborne measurements of the sea surface salinity (SSS). In this paper, we present examples demonstrating how SMOS-derived SSS data are being used to better characterize key land–ocean and atmosphere–ocean interaction processes that occur within the marine hydrological cycle. In particular, SMOS with its ocean mapping capability provides observations across the world's largest tropical ocean fresh pool regions, and we discuss from intraseasonal to interannual precipitation impacts as well as large-scale river runoff from the Amazon–Orinoco and Congo rivers and its offshore advection. Synergistic multi-satellite analyses of these new surface salinity data sets combined with sea surface temperature, dynamical height and currents from altimetry, surface wind, ocean color, rainfall estimates, and in situ observations are shown to yield new freshwater budget insight. Finally, SSS observations from the SMOS and Aquarius/SAC-D sensors are combined to examine the response of the upper ocean to tropical cyclone passage including the potential role that a freshwater-induced upper ocean barrier layer may play in modulating surface cooling and enthalpy flux in tropical cyclone track regions.

Keywords: Sea surface salinity ; SMOS satellite ; Passive microwave remote sensing ; Oceanic freshwater cycle

1. Introduction

Salinity is known to play an important role in the dynamics of the ocean's thermohaline overturning circulation and in large-scale atmosphere–ocean climate signals such as the El Niño Southern Oscillation (ENSO), and is the key freshwater tracer within the oceanic component of the global hydrologic cycle, a branch that comprises most of the global precipitation and evaporation as well as the river runoff (Schmitt 2008). Multi-decadal sea surface salinity (SSS) trends have been documented in tropical and high latitudes and associated with signatures of evaporation or precipitation variation that are consistent with global warming scenarios (e.g., Dickson et al. 2002; Gordon and Guillivi 2008; Morrow et al. 2008; Cravatte et al. 2009; Yu 2011; Durack et al. 2012; Terray et al. 2011). These studies highlight the need for well-sampled SSS time series both for

70 monitoring the change and to improve basic understanding of the respective roles of the
71 atmosphere and ocean dynamics, thermodynamics, air–sea interaction, and land-ocean
72 interaction in the global water cycle context.

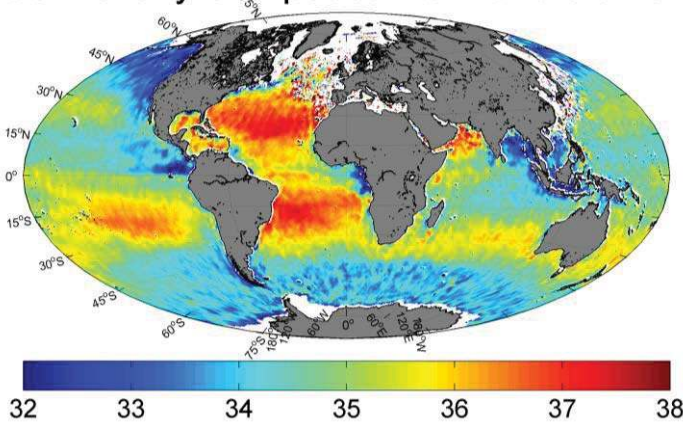
73 Our basic knowledge of the global SSS distribution is derived from the compilations of all
74 available oceanographic data collected over time (e.g. Boyer and Levitus, 2002). The SSS
75 in situ observing system has expanded significantly during the last decade due mostly to
76 the full deployment of the Argo profiling float array, and now provides a monthly SSS
77 estimate on a grid of roughly 300-400 km². Notwithstanding these recent gains, this
78 sampling density is still too sparse to resolve climatologically important intraseasonal,
79 seasonal, and interannual to decadal signals at the 300 km spatial scale within which SSS is
80 known to vary significantly (Lagerloef et al, 2010). The recent launch of the ESA/SMOS
81 (Soil Moisture and Ocean Salinity, see Kerr et al., 2010; Font et al., 2010) and
82 NASA/Aquarius SAC-D (Lagerloef et al., 2008; Lagerloef et al., 2012) mission satellites
83 represent contributions towards filling this gap using passive microwave remote sensing.

84 Salinity remote sensing is based on measurement of sea surface microwave
85 emission at the lower end of the microwave spectrum and from a surface skin layer having
86 a thickness of $O(1\text{ cm})$. This emission depends partly on the dielectric constant of sea
87 water, which in turn can be related to salinity and temperature. Thus, given sea surface
88 temperature (SST), theory predicts some ability to invert SSS information. In practice
89 however, numerous additional external factors (extra-terrestrial sources, atmosphere,
90 ionosphere and surface roughness) also contribute to the satellite-observed emission and
91 these must be corrected to allow accurate ocean salinity estimates. The SMOS and
92 Aquarius sensors are both ocean microwave radiometers operating at a frequency of ~1.4
93 GHz (L-band, wavelength of 21 cm), a band chosen for the relatively strong sensitivity to
94 change in salinity and because this is a transmission-free, or protected, frequency. An
95 additional and important benefit for this choice is minimization of atmospheric signal
96 contributions.

97 Based on observed SSS variability and need to better resolve it, the satellite missions aim
98 to produce salinity estimates with an accuracy of 0.1–0.2 over the so-called Global Ocean
99 Data Assimilation Experiment (GODAE) scales of 100 km, one month or 200 km, and 10
100 days. This is a challenging objective for several reasons. First, the sensitivity of L-band
101 brightness temperatures to variations in SSS is on average 0.5 degK per salinity unit. This
102 sensitivity is very weak given that spatial and temporal variability in open-ocean SSS does
103 not exceed several units and that the instrument noise is typically 2–5 degK. Second, there

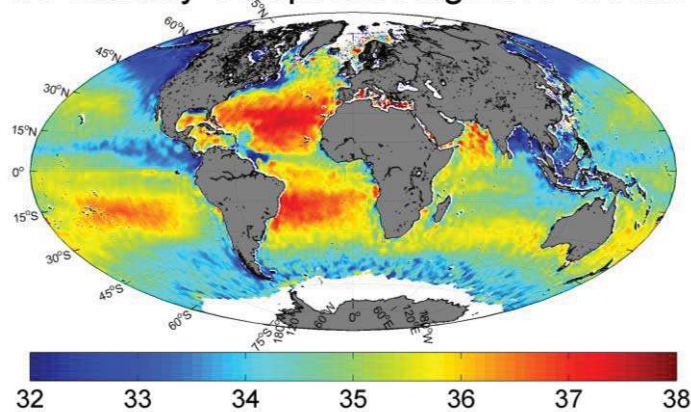
104 are many geophysical sources of brightness at L-band that corrupt the salinity signal, and
105 correction models for these factors have uncertain accuracy. Moreover, the technical
106 approach developed in order to achieve adequate radiometric accuracy and spatio-temporal
107 resolution for SMOS is polarimetric interferometric radiometry, the first such spaceborne
108 system. The complex SMOS image reconstruction data processing includes contamination
109 by different errors and induces residual inaccuracies in SSS estimates. Finally, there is
110 significant radio frequency interference emanating from sources along the many coastlines
111 that contaminate data collected over many ocean regions. Nevertheless, much work at
112 ESA SMOS Level 2 expert centers and the CNES/IFREMER Centre Aval de Traitement
113 des Données SMOS (CATDS) has addressed these issues, leading to the first global
114 satellite SSS estimates (Font et al. 2012, Reul et al. 2012, Boutin et al. 2012a).
115

SSS Monthly Composite Mar 2010-0.5°x0.5°



116

SSS Monthly Composite Aug 2010-0.5°x0.5°



117

118 **Figure. 1** Monthly composites of the sea surface salinity at a spatial resolution of
119 0.5°x0.5° deduced from SMOS data (CATDS v2) for the months of March (top) and August
120 (bottom) 2010.

121

122

123 Two examples of monthly composite SMOS SSS maps are shown in Figure 1. They show
124 salient basin scale features, including the elevated salinity in the Atlantic relative to the
125 other basins, and the general correspondence of lower SSS with known river runoff and
126 tropical precipitation regions. SMOS data validation efforts using *in situ* observations
127 reveal an overall SSS accuracy on the order of 0.3 (Boutin et al., 2012a; Reul et al., 2012;
128 Bank et al., 2012; Font et al., 2013), but with degraded quality at high latitudes partly
129 because of reduced sensitivity in colder waters. While further improvements are in
130 progress, many interesting features of the global SSS could be already evidenced.

131

132 This paper reviews preliminary results addressing several key applications of these new
133 satellite SSS data. Given the reduced SMOS sensitivity in colder waters, the focus is on
134 tropical ocean data where SMOS measurements have proven to be the most accurate. We
135 also attempt to highlight combined use of other satellite and *in situ* observations (altimetry,
136 SST, ocean color, river discharge, evaporation, precipitation). It is shown that these new
137 data are proving useful in the monitoring of intraseasonal to interannual variability across
138 major Tropical freshwater pools of the world ocean. SMOS-detected SSS freshening
139 events within intense precipitation zones (e.g., the Inter-Tropical Convergence Zone) are
140 also shown to provide promising new information related to the ocean surface response to
141 rainfall. Finally, SMOS SSS data are used to address interactions between wind-driven
142 phenomena, such as upwelling and Tropical cyclones, and some of the world largest Fresh
143 pools. The datasets used in these cases are described in Section 2. SMOS monitoring
144 capabilities for the major tropical river plumes are given in Section 3. In sections 4 and 5,
145 we illustrate rain impacts detected in SMOS SSS data then their application improved
146 understanding of freshwater pools interaction with the atmosphere. Conclusions and
147 perspectives are given in section 6.

148

149 **2. Data**

150

151 A range of satellite and *in situ* datasets are used in the present study with focus on the years
152 2010-2011 following the SMOS launch date. The data products are described below.

153

154 **2.1 SMOS SSS data**

155 SMOS (Soil Moisture and Ocean Salinity) is the European Space Agency (ESA)'s water
156 mission (Kerr et al. 2010; Mecklenburg et al. 2012), an Earth Explorer Opportunity

157 Mission approved under the Living Planet Program. SMOS was launched in November
 158 2009 and the technical approach developed to achieve adequate radiometric accuracy, as
 159 well as spatial and temporal resolution compromising between land and ocean science
 160 requirements, is polarimetric interferometric radiometry (Ruf et al. 1988; Font et al. 2010)
 161 at L-band (frequency of ~1.4 GHz). ESA produces so-called Level 2 SSS, or L2 products
 162 which correspond to instantaneous SSS retrievals under the satellite swath.

163 **Table 1:** Summary of characteristics of CATDS-CEC SSS level 3 products

	CEC IFREMER	CEC LOCEAN
SSS retrieval method	SSS retrieved from first Stokes parameter (Reul and Tenerelli 2011)	SSS retrieved from polarized Tbs along dwell-lines using an iterative retrieval (see ESA L2OS ATBD)
Region of the instrument field of View (FOV) considered for SSS retrieval	Alias Free Field of View only	Alias Free Field of View (AFFOV) and extended AFFOV along dwell lines with at least 130 Tb in AFFOV (~ +/-300km from the swath center)
Tb sortings	Determined from interorbit consistency in incidence angles classes and thresholding	Determined from consistency along dwell lines as reported in ESA level 2 products
Galactic model	Geometrical optics model	Kirchoff Approx. scattering at 3m/s
Roughness/foam models	Empirical adjustment of Tb dependencies to wind speed	Empirical adjustment of parameters in roughness model and foam coverage models (Yin et al. 2012)
Calibration	Single Ocean Target Transformation (OTT) + daily 5°x5° adjustment wrt World Ocean 2001 SSS climatology	Variable OTT (every 2 weeks synchronised with Noise Injection Radiometer as defined in ESA reprocessing)
Average	Simple average	Average weighted by theoretical error on retrieved SSS and spatial

		resolution
--	--	------------

164

165 In the present study, level 2 SMOS SSS are from the first SMOS/ESA annual reprocessing
 166 campaign in which ESA level 1 v5.04 and level 2 v5.50 processors have been used. In these
 167 versions, significant improvements with respect to the flaws discovered in the first
 168 products (e.g. Reul et al., 2012) have been implemented (see a complete description in the
 169 Algorithm Theoretical Basis Document (ATBD) available at
 170 <http://www.argans.co.uk/smos/docs/deliverables/>). Nevertheless, accuracy of these
 171 instantaneous SSS retrievals is rather low (~0.6-1.7 unit) and space-time averaging of the
 172 Level 2 products is needed (so-called Level 3 SSS) to decrease the noise level in the
 173 retrievals.

174 Here we used two types of composite SSS level 3 products generated in
 175 laboratories participating to the Expertise Center of the Centre Aval de Traitement des
 176 Données SMOS (CATDS, <http://www.catds.fr>), which is the french ground segment for
 177 the SMOS data. These products are built either from ESA level 1 products (Reul and
 178 Tenerelli, 2011) or from ESA level 2 products (Boutin et al, 2012b).

179 These research products aim at assessing the quality of SMOS operational products
 180 (ESA level 2 and CATDS-OP level 3) and at studying new processings to be implemented
 181 in the future in operational chains. Main characteristics of these products are detailed in
 182 Table 1. CEC-IFREMER products have been used in section 3 & 5, CEC-LOCEAN
 183 products in section 4.

184 Overall accuracy of the 10-days composite products at 25 km resolution is on the order of
 185 0.3 practical salinity unit in the tropical oceans (Reul and Tenerelli, 2011). Note
 186 that salinity computations are based on the Practical Salinity Scale PSS-78, and reported
 187 with no units (United Nations Educational, Scientific and Cultural Organization, 1985).

188

189 **2.2 Ocean Surface Currents**

190 Here we used the 1/3° resolution global surface current products from Ocean Surface
 191 Current Analyses Realtime (OSCAR) (Bonjean and Lagerloef, 2002;
 192 <http://www.oscar.noaa.gov>), directly calculated from satellite altimetry and ocean vector
 193 winds.

194 The OSCAR data processing system calculates sea surface velocities from satellite
 195 altimetry (AVISO), vector wind fields (QuikSCAT), as well as from sea surface

196 temperature (Reynolds-Smith) using quasi-steady geostrophic, local wind-driven, and
197 thermal wind dynamics. Near real time velocities are calculated on both a $1^\circ \times 1^\circ$ and
198 $1/3^\circ \times 1/3^\circ$ grid on a ~5 day time base over the global ocean. Surface currents are provided
199 on the OSCAR website (<http://www.oscar.noaa.gov>) starting from 1992 along with
200 validations with drifters and moorings. The $1/3^\circ$ resolution is available for ftp download
201 through <ftp://ftp.esr.org/pub/datasets/SfcCurrents/ThirdDegree>.

202

203 **2.3 Rain, Evaporation and River Discharge data**

204 To estimate the rain-rate over the oceans, we used three different satellite products.

205 One is the monthly TRMM Composite Climatology (TCC) of surface precipitation
206 based on 13 years of data from the Tropical Rainfall Measuring Mission (TRMM). The
207 TCC takes advantage of the information from multiple estimates of precipitation from
208 TRMM to construct mean value maps over the tropics ($36^\circ\text{N} - 36^\circ\text{S}$) for each month of the
209 year at 0.5° latitude-longitude resolution. The first-time use of both active and passive
210 microwave instruments on board TRMM has made it the foremost satellite for the study of
211 precipitation in the tropics and has led to a better understanding of the underlying physics
212 and distribution of precipitation in this region. The products are available at NASA
213 Goddard Space Flight Center Global Change Master Directory (<http://gcmd.nasa.gov>).

214 The second type of satellite rain rate estimates that we used in the present study are the
215 so-called ‘TRMM and Other Satellites’ (3B42) products, obtained through the
216 NASA/Giovanni server (<http://reason.gsfc.nasa.gov/OPS/Giovanni>). The 3B42 estimates
217 are 3-hourly at a spatial resolution of 0.25° with spatial extent covering a global belt
218 (-180°W to 180°E) extending from 50°S to 50°N latitude. The major inputs into the 3B42
219 algorithm are IR data from geostationary satellites and Passive Microwave data from the
220 TRMM microwave imager (TMI), special sensor microwave imager (SSM/I), Advanced
221 Microwave Sounding Unit (AMSU) and Advanced Microwave Sounding Radiometer-
222 Earth Observing System (AMSR-E).

223 The Special Sensor Microwave Imager (SSM/I) F16 and F17 orbits cross SMOS
224 orbits within -20 min and +40 min. Hence, numerous SMOS level 2 are collocated with
225 SSMI rain rates (RR) within this range of time. In addition to the TRMM 3B42 products,
226 we therefore used SSM/Is datasets to perform co-locations between SMOS SSS and rain
227 estimates. SSM/Is RR version 7 were used and downloaded from <http://www.remss.com>.

228 The evaporation (E) data set was taken from the Version 3 products of the
229 Objectively Analyzed air-sea Fluxes (OAFlux) project (Yu and Weller, 2007).

230 Finally the discharge data for the Amazon, Orinoco and Congo rivers were obtained
231 from the Environmental Research Observatory (ORE) HYBAM (Geodynamical,
232 hydrological and biogeochemical control of erosion/alteration and material transport in the
233 Amazon basin) website.

234

235 **2.4 Ocean Color products**

236 To study the spatio-temporal coherency between SSS signals from some major tropical
237 river plumes and ocean color properties, we used the level-3 daily, 4-km resolution
238 estimates of the absorption coefficient of colored detrital matter (CDM) at 443 nm. These
239 products processed and distributed by ACRI-ST GlobColour service, are supported by the
240 EU FP7 MyOcean2 and the ESA GlobColour Projects, using ESA ENVISAT MERIS data,
241 NASA MODIS and SeaWiFS data. These products have been averaged at the SMOS L3
242 product 0.25° resolution, with a 10-days running mean.

243

244 **2.5 In situ data**

245 Salinity measurements from Argo floats are provided by the Coriolis data centre
246 (<http://www.coriolis.eu.org/>). The upper ocean salinity values recorded between 4m and
247 10m depth will be referred to as Argo SSS following Boutin et al. (2012b).

248 Global SSS maps are derived from delayed time quality checked in situ measurements
249 (Argo and ship) by IFREMER/LPO, Laboratoire de physique des oceans, using the In Situ
250 Analysis System (ISAS) optimal interpolation (D7CA2S0 re-analysis product) (see a
251 method description on [http://wwz.ifremer.fr/lpo/SO-Argo-France/Products/Global-Ocean-](http://wwz.ifremer.fr/lpo/SO-Argo-France/Products/Global-Ocean-T-S/Monthly-fields-2004-2010)
252 [T-S/Monthly-fields-2004-2010](http://wwz.ifremer.fr/lpo/SO-Argo-France/Products/Global-Ocean-T-S/Monthly-fields-2004-2010) and in (Gaillard et al., 2009)). The choice for the time and
253 space scales used in that method results from a compromise between what is known of
254 ocean time and space scales and what can actually be resolved with the Argo array (3°, 10
255 days); two length-scales are considered: the first one is isotropic and equal to 300 km, the
256 second one is set equal to 4 times the average Rossby radius of deformation of the area. As
257 a result, we expect these maps being smoother, especially in tropical areas, than SMOS
258 SSS maps averaged over 0.25°x0.25° or 1° x1°.

259

260 **3. SMOS monitoring of the Major Tropical Atlantic River** 261 **Plumes**

262 Rivers are important variables in oceanography as their fresh water affects SSS and
263 the buoyancy of the surface layer, and they represent a source of materials exotic to the

264 ocean and important to biological activity. Obviously, they are key hydrologic
265 components of the fresh water exchanges between land and ocean. Despite this importance,
266 tracing major tropical river water (e.g. Amazon, Congo, Ganges) over large distances has
267 not been straightforward previously principally because of a lack of SSS observations.
268 Tracing those very large rivers over great distances now become an important endeavor, as
269 sufficient data are available from surface salinity sensors placed aboard satellites.

270 Occurrence of patches of low surface salinity (< 35 practical salinity units) in the
271 Tropical Atlantic Ocean is closely related to the presence of the mouths of the world's
272 largest rivers in terms of fresh-water discharge (e.g. Amazon, Congo, Orinoco) and their
273 subsequent spreading of fresh water by the upper ocean circulation. Another key fresh
274 water source here is the Inter Tropical Convergence Zone (ITCZ), associated with
275 relatively intense precipitation that migrates latitudinally over the tropical Atlantic
276 throughout the year (Binet and Marchal 1993). One of these major low salinity pools is
277 formed by the Amazon and Orinoco river plumes spreading offshore from the South
278 America north-eastern coasts, and influencing a large fraction of the western tropical North
279 Atlantic (Neumann, 1969; Lentz 1995; Muller-Karger et al. 1988; Dessier and Donguy,
280 1994). The Gulf of Guinea, situated in the North-Eastern Equatorial Atlantic (NEEA) is
281 also an important location for the fresh water budget in the tropical Atlantic. It is a region
282 of intense precipitation with as much as 30 cm of rain falling per month during the rainy
283 season (Yoo and Carton [1988]). Furthermore, into this area flows the Congo River, the
284 largest fresh water input to any eastern ocean boundary. These large-scale low salinity
285 'lenses' at the Tropical Atlantic surface can be traced over distances ranging from several
286 hundreds up to thousands of kilometers in the upper ocean. They are characterized by very
287 distinct and in general strong seasonally varying spatial extents.

288

289 **3.1 Amazon and Orinoco River Plume monitoring**

290

291 The Amazon is the world's largest river in terms of fresh water discharge (Milliman
292 and Meade, 1983; Perry et al. 1996). It drains a large fraction of the South American
293 continent, discharging on average $1.55 \pm 0.13 \times 10^5 \text{ m}^3 \text{ s}^{-1}$ of fresh water into the equatorial
294 Atlantic Ocean (Perry et al. 1996). This is about 15% of the estimated global river discharge
295 on an annual basis. The Amazon River is by far the largest single source of terrestrial fresh
296 water to the ocean and contributes about 30% of total river discharge to the Atlantic Ocean
297 (Wisser et al., 2010). The structure of the Amazon plume is strongly influenced by a

298 variety of physical processes which are present on the northern Brazilian shelf: the North
299 Brazil Current (Flagg et al., 1986; Richardson and McKee, 1984), trade winds (Hellerman
300 and Rosenstein, 1983) and strong currents associated to the tide (Nittrouer and Demaster,
301 1986). These physical processes play a very significant role in the dispersal and spreading
302 of Amazon discharge (fresh water and suspended sediment) on the northern continental
303 shelf of South America.

304

305 Previous studies have shown that Amazon Plume water can be traced offshore and
306 northwestward along the north Brazilian coast, covering most of the continental shelf from
307 11°S to 5°N (Muller-Karger et al. 1988, 1995) into the Caribbean (e.g. Steven and Brooks
308 1972; Froelich et al.1978; Hellweger and Gordon, 2002; Cherubin and Richardson,2007),
309 and over 1000 km eastward into the North Atlantic depending on the season. Beyond this
310 region, the Amazon's water has been traced northwestward into the Caribbean Sea and
311 eastward in the North Atlantic (Muller-Karger et al. 1988, 1995; Johns et al., 1990;
312 Hellweger and Gordon, 2002). Hydrographic surveys by Lentz and Limeburner (1995)
313 revealed that the Amazon Plume over the shelf is typically 3-10m thick and between 80 and
314 >200 km wide. Beyond the shelf, fresh water within the plume gradually attenuates with
315 depth as it travels away from the source, with a penetration depth of 40m to 45m as far as
316 2600 km offshore (Hellweger and Gordon, 2002; Hu et al., 2004).

317 Both chlorophyll (Chl) concentration and primary productivity are greatest in the river
318 plume-ocean transition zone, where the bulk of heavy sediments are deposited (Smith and
319 Demaster, 1996). The combination of riverine nutrient input and increased irradiance
320 availability creates a highly productive transition zone, the location of which varies with
321 the discharge from the river. High phytoplankton biomass and productivity of over 25 mg
322 Chl-a m⁻³ and 8 g Cm⁻² d⁻¹, respectively, are found in this transition region (Smith and
323 Demaster, 1996). Because of this, the North Brazil shelf acts as a significant sink for
324 atmospheric CO₂ (Ternon et al., 2000).

325

326 The north western Tropical Atlantic is also an area where another major river in the world,
327 the Orinoco, enters the ocean. The Orinoco River originates in the southern part of
328 Venezuela, and discharges waters from about 31 major and 2000 minor tributaries into the
329 western tropical Atlantic. These waters are most of the time transported into the
330 southeastern Caribbean sea and during the rainy season a larger but unquantified fraction
331 of the plume also flows east around Trinidad and Tobago into the Caribbean. The Orinoco

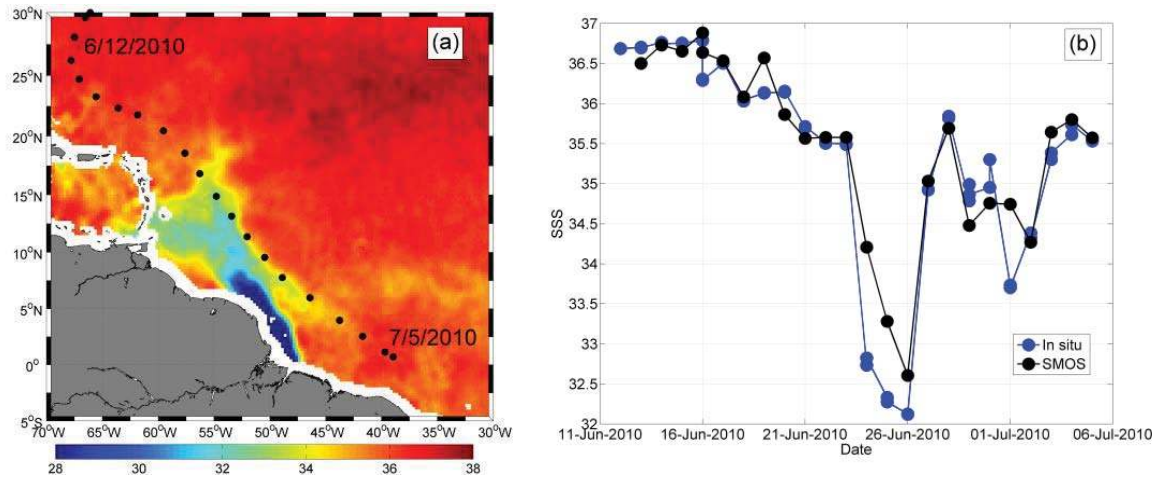
332 is considered to be the third largest river in the world in terms of volumetric discharge
333 (after the Amazon and the Congo), discharging an average of $\sim 3.6 \times 10^4 \text{ m}^3 \text{ s}^{-1}$ (Meade et
334 al., 1983; Muller-Karger et al., 1989; Vörösmarty et al., 1998). Low discharge occurs
335 during the dry season (January–May) and high discharge during the rainy season (July–
336 October) as a result of the meridional migration of the ITCZ.

337

338 The fresh water discharges from the Amazon and Orinoco Rivers spread outward into the
339 western equatorial Atlantic Ocean while continually mixing with surrounding salty ocean
340 surface water. The averaged geographical distribution of the low-salinity signatures of the
341 Amazon and Orinoco River plumes can be revealed with historical in situ surface salinity
342 data. However, only satellite remote sensing data is known to provide means to monitor the
343 wide surface dispersal of these two fresh pools, with ocean color data being the first to
344 illustrate Amazon plume reach to well beyond 1000 km (Muller Karger et al., 1988). Since
345 these first observations, the application of ocean color, altimetry, and SST satellite
346 mapping in this region has increased in its sophistication, showing the ability to track
347 surface plume area (e.g. Hu et al., 2004; Moller et al., 2010), fronts along the shelf to the
348 North West (Baklouti et al., 2007), and northward propagating eddies or waves shed near
349 the North Brazil Current (NBC) retroreflection region, the so-called NBC rings (Field,
350 2005; Goni and Johns, 2001; Garzoli et al., 2004). In each case, the satellite data are able
351 to provide time-resolved information on advective processes up to certain limits that
352 include cloud cover, minor SST and ocean color gradients, non-conservative dilution
353 processes for the ocean color to salinity conversions (Salisbury et al., 2011), and
354 baroclinicity and subgrid variability of the altimetry Seas Surface Height Anomaly (SSHA)
355 tracking of the NBC rings. As first evidenced by Reul et al., 2009, passive remote sensing
356 data at low microwave frequencies can be successively used to complement these more
357 'classical' satellite observations to better follow the temporal evolution and spatial
358 distribution of surface salinity within and adjacent to the Amazon River Plume.

359 To illustrate this new capability, we first show in Figure 2 comparisons between
360 collocated SMOS SSS and *in situ* Conductivity-Temperature Depth (CTD) measurements
361 acquired during the Geotraces West Atlantic cruise leg 2 across the Amazon river plume in
362 June 2010. This campaign was conducted on RV Pelagia in the frame of the GEOTRACES
363 international program (see <http://www.geotraces.org/>).

364



365

366 **Figure 2:** (a) Black dots: location of the CTD stations conducted during the Geotraces
 367 West Atlantic cruise leg 2 (RV Pelagia) from 11 June to 5 July superimposed on the SMOS
 368 averaged SSS from June 12th to July 5th 2010. (b) Co-located surface salinity between
 369 SMOS and in situ data along the leg. SMOS data have been averaged at 50 km resolution
 370 with a ± 5 days running temporal window.

371

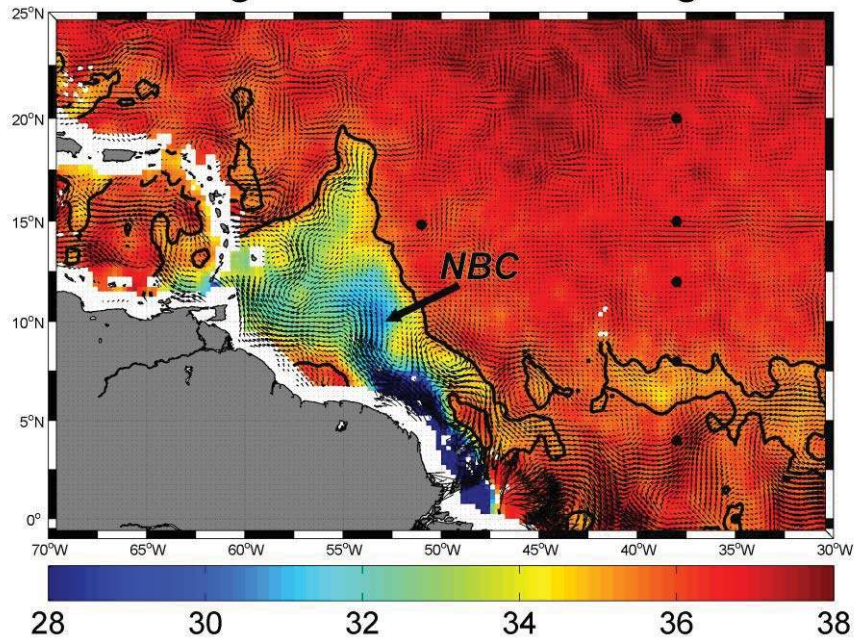
372 Comparison between satellite and 3-m depth *in situ* SSS data reveals an overall good
 373 agreement with a standard deviation of the difference $SSS_{SMOS} - SSS_{CTD}$ of ~ 0.45 . In
 374 particular, the strong gradient and ~ 3 unit drop observed as the R/V Pelagia leg crossed the
 375 Amazon river plume is well detected by the satellite observations.

376 New sea surface salinity products from satellite platforms such as SMOS allow in
 377 particular to gain insights into the advection pathways of the fresh water Amazon and
 378 Orinoco river plume along surface currents. For the first time, SMOS sampling capability
 379 thus enables imaging the plume structure almost every 3 days with a spatial resolution of
 380 about 40 km. Combining SMOS SSS with altimeter-derived geostrophic currents and
 381 wind-driven (Ekman) estimated motions (Lagerloef et al., 1999), the advection of the
 382 spatial patterns of low salinity discharged from the major river mouths can now be
 383 analyzed systematically with an unprecedented resolution.

384 As illustrated by the Figure 3 and by the animation available at
 385 http://www.ifremer.fr/naiad/salinityremotesensing.ifremer.fr/altimetry_amazon_atl.gif,
 386 a very good visual consistency is found between the geostrophic and Ekman surface
 387 current pattern estimates and the SMOS SSS spatio-temporal distribution along the year.

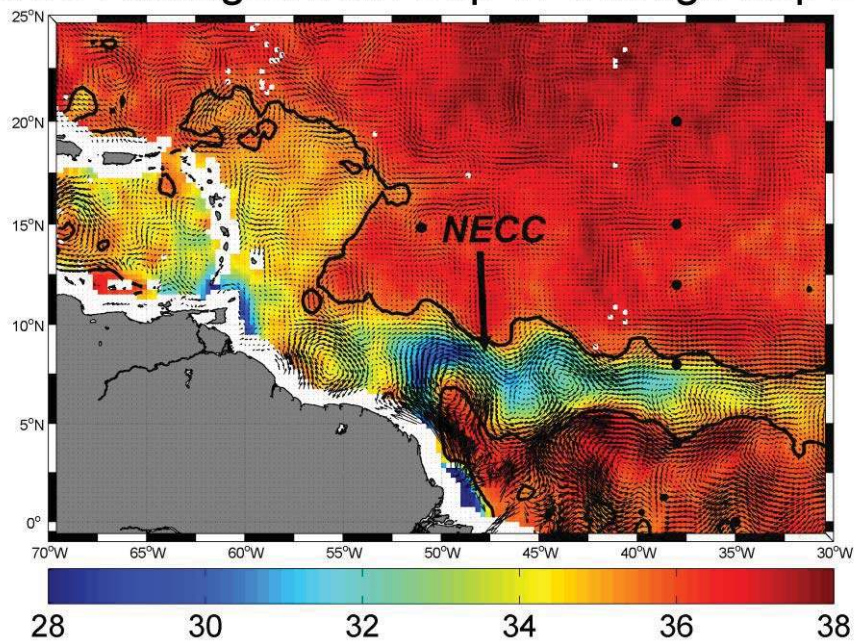
388

SSS Averaged from Jun 04 through Jun 14



389

SSS Averaged from Sep 17 through Sep 27



390

391 **Figure.3** Major pathways for the freshwater Amazon-Orinoco river plume detected by
392 SMOS in 2010. Surface salinity fields from SMOS are superimposed with coinciding
393 surface OSCAR currents estimated from altimetry and surface wind data. Top: the
394 freshwater Amazon river plume is advected northwestward along the Brazilian Shelf by the
395 North Brazilian Current (NBC) during boreal spring. Bottom: during boreal summer to
396 fall period, the Amazon plume is carried eastward by the North Equatorial Counter
397 Current (NECC). Note also the signal from the Orinoco river plume extending
398 Northeastward along the southern lesser Antilles. In both plots the thick black curve is
399 indicating the 35 SSS contour.

400

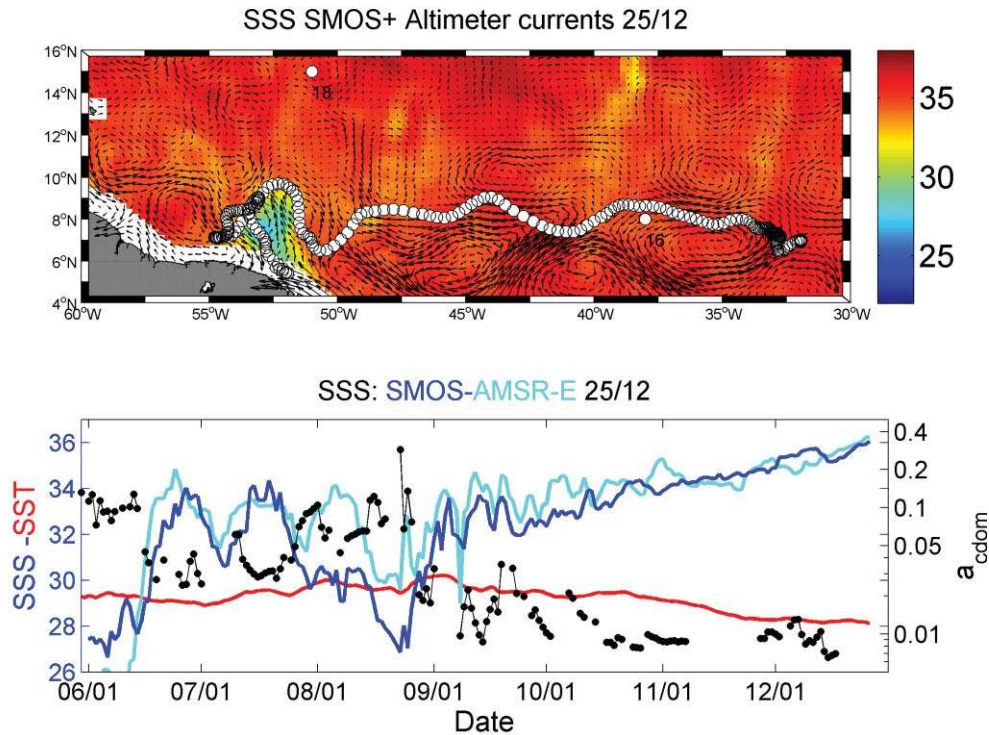
401 Mignot et al. (2007) show a long-term seasonal to monthly climatology that highlights two
402 fresh water offshore pathways - the north passage to the warm pool and eastward

403 entrainment into the North Equatorial Counter Current (NECC) – but they cannot clearly
404 confirm or track this laterally with time in a given year.

405 SMOS SSS data combined with altimetry and surface wind information now enable to
406 follow the spatio-temporal evolution of the plume along these twofresh water offshore
407 pathways.

408 As illustrated in Figure 3 (top), the surface fresh water dispersal patterns of the Amazon
409 river plume are closely connected to the surface current topology derived from the merged
410 altimeter and wind field product. As also evidenced earlier from several hydrographic
411 surveys (e.g., Hellweger and Gordon, 2002), it is clearly apparent in the satellite imagery
412 that the NBC rings are key factors in modulating the fresh water pathways of the Amazon
413 plume from the river mouth at the equator towards higher latitudes up to 20°-22°N.

414 Eastward entrainment of low salinity water from the mouth of the Amazon river into the
415 North Equatorial Counter Current (NECC) is also evident in the SMOS data for the
416 second half of the year 2010 (see Figure 3, bottom). During that period, fresh water
417 dispersal structure exhibits a zonal wavy pattern centered around ~8°N induced by current
418 instability waves shed near the North Brazil Current (NBC) retroflection region
419 (52°W,8°N). To analyze the freshwater plume transport and the evolution of salinity along
420 Lagrangian paths following such wavy patterns, hypothetical drifters were dropped around
421 the mouth of the river at the beginning of June and temporally advected with the surface
422 currents deduced from merged altimeter and wind products. The evolution of sea surface
423 salinity from SMOS L-band and AMSR-E C-band sensors (see Reul et al., 2009 for details
424 on the AMSR-E SSS product), sea surface temperature analysis products and merged
425 MERIS-MODIS Colored Dissolved Organic Matter (CDOM) absorption coefficient was
426 estimated by interpolating the data in space and time along the path of such drifters.



427

428 **Figure 4:** Top: spatio-temporal evolution of the location of an hypothetical drifter (white
 429 dots) dropped at 52°W6°N at the beginning of June 2010 and advected with surface
 430 currents estimated from altimetry & surface winds (arrows). Superimposed are the +/-5
 431 days averaged daily SSS fields from SMOS and the surface currents (black arrows).
 432 Bottom: time series of the co-localized SSS from SMOS (blue) and from AMSR-E (cyan),
 433 the analyzed SST (red), and the merged daily CDOM (black) along the drifter path.

434

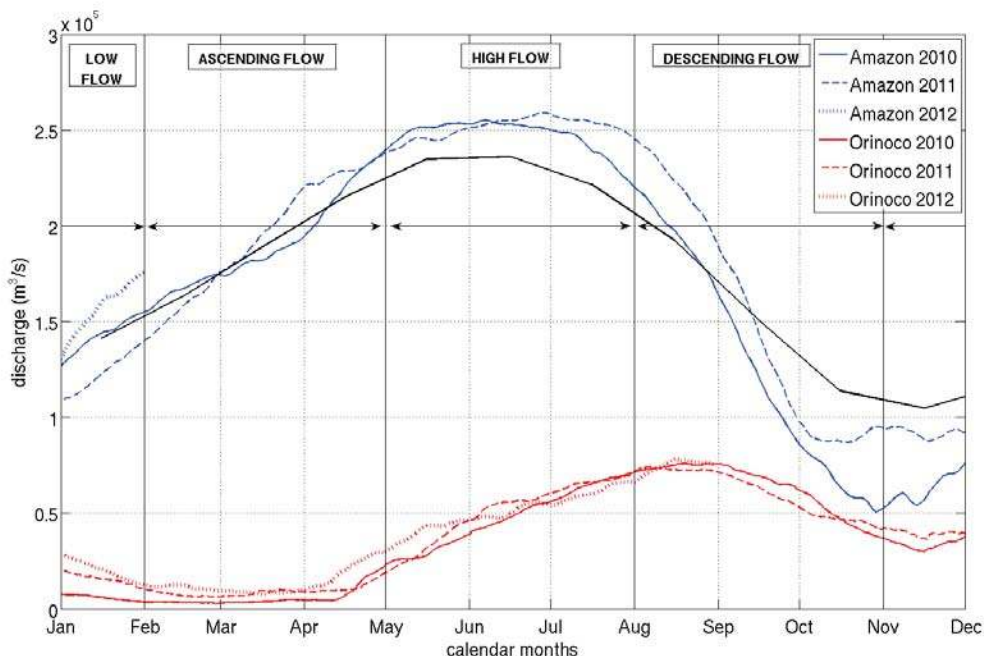
435 As further illustrated by the example shown in Figure 4, it takes approximately 6 months to
 436 cover a distance of 3700 km for a fresh water particle (SSS~26-28) in the proximity of the
 437 Amazon mouth to relax to an open ocean surface salinity of ~36. At the beginning of the
 438 period, the low SSS of water particles is modulated by mixing processes with saltier
 439 waters transported westward by the NBC rings shed at the NBC retroflection. The particle-
 440 following SSS signal modulation observed here is clearly consistent with the ocean color
 441 signal (anti-correlated to SSS), fresher water being systematically associated with colored
 442 waters showing high CDOM values, typical of the brackish plume waters. The drifter is
 443 then advected eastward along the NECC, remixed with 'younger' advected plume waters in
 444 August and reached an eastern position slightly north of 8°N-38°W with an SSS of about
 445 32 at the beginning of October. The SSS change along the drifter pathway is progressively
 446 and quasi-linearly relaxing to the open ocean values during the next 3-month period.

447

448 The link between the SSS and ocean color properties moreover enables investigations of
 449 the interactions between bio-optical and bio-chemical properties of the ocean and

450 hydrological fluxes of terrestrial origin. Along with the fresh water, the Amazon provides
 451 the largest riverine flux of suspended (1200 Mt y^{-1}) and dissolved matter (287 Mt y^{-1}),
 452 which includes a dissolved organic matter (DOM) flux of 139 Mt y^{-1} (Meybeck and Ragu
 453 1997). These fluxes can have a dramatic effect on regional ecology as they represent
 454 potential subsidies of organic carbon, nutrients, and light attenuation into an otherwise
 455 oligotrophic environment (Muller-Karger et al., 1995).

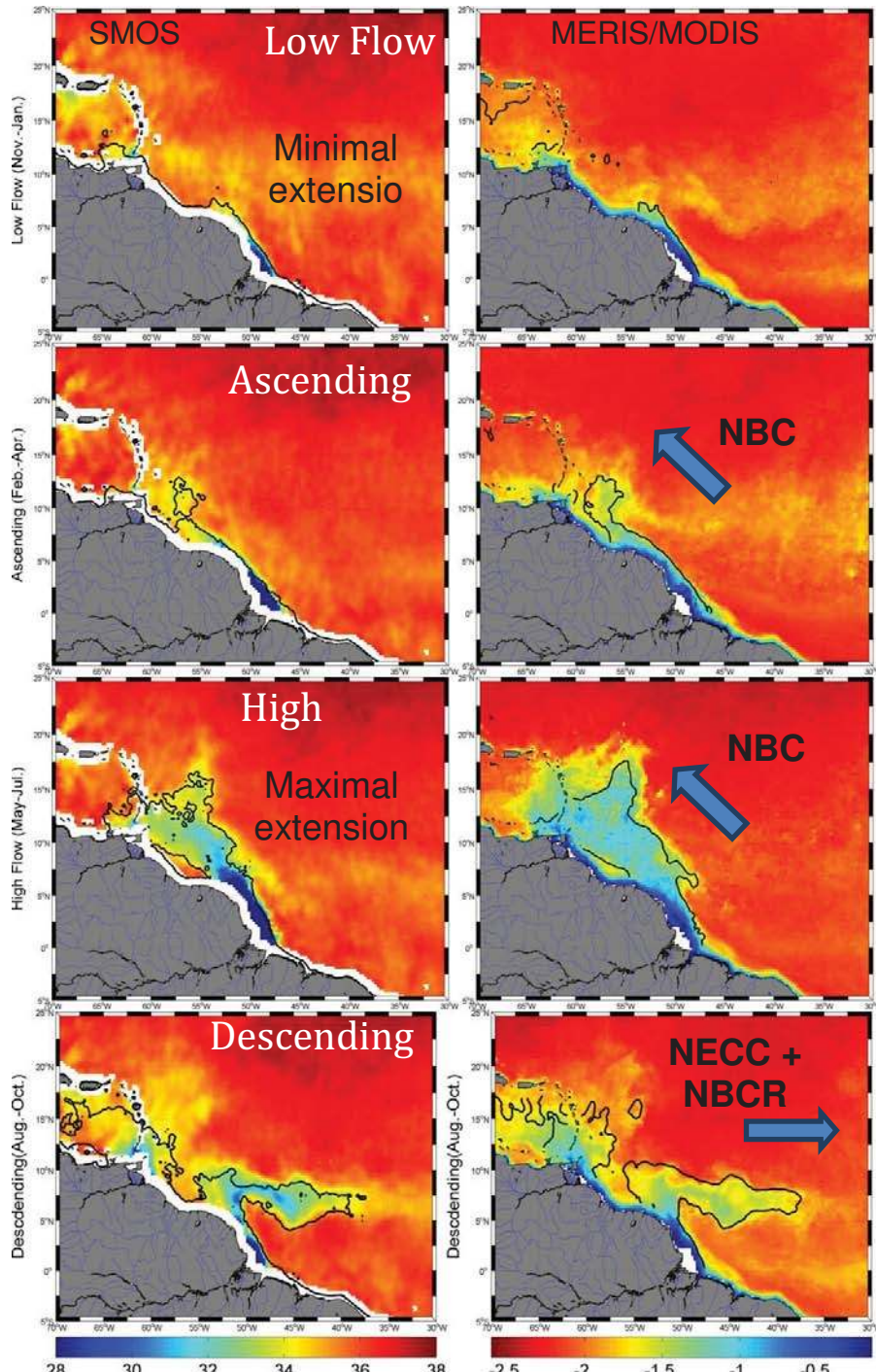
456 In the most proximal regions of the Amazon Plume, light attenuation by suspended
 457 detritus acts as the main limitation to phytoplankton growth (Demaster and Smith, 1996).
 458 Away from this region, as mineral detritus is removed by sinking, absorption attributable
 459 to organic substances begins to dominate the attenuation of light in surface waters.
 460 DelVeccio and Subramaniam (2004) studied such conditions in the Amazon Plume and
 461 characterized the relative contributions of CDOM, particulate organic material and
 462 phytoplankton to the total absorption field. In the coastal ocean adjacent to river sources,
 463 CDOM tends to behave as a fresh water tracer, decreasing away from the river source with
 464 increasing salinity. Linear correlations between CDOM and salinity in river plume waters
 465 are well documented in ocean color literature with reported relationships robust enough to
 466 allow salinity retrievals from CDOM and vice versa (e.g. Ferrari and Dowell, 1998;
 467 Palacios et al., 2009; D'Sa et al., 2002; Conmy et al., 2004).



468
 469 **Figure 5:** Amazon (blue) and Orinoco (red) River discharge cycles measured respectively
 470 at Obidos and Bolivar gauges, during the period 2010- 2012. The black curve is showing
 471 the Amazon river discharge climatology from 1968 to 2012.
 472

473 Linearity in the CDOM – salinity relationship implies conservative mixing dominated by
474 two distinct endmembers. Departures from linearity can occur when additional water
475 masses are present (Blough and Delveccio, 2002), or by *in situ* subsidies of CDOM
476 released via net phytoplankton growth (Yamashita and Tanoue, 2004; Twardoski and
477 Donaghay, 2001), microbial utilization (e.g. Moran et al., 1999; Obernosterer and Herndl,
478 2000), or photochemical oxidation (e.g. Miller and Zepp, 1995).

479 Based upon preliminary satellite microwave SSS data from AMSR-E sensor and ocean
480 color products, Salisbury et al., (2011) recently demonstrated the spatial coherence
481 between surface salinity and the absorption coefficient of CDOM at 443 nm in the Amazon
482 and Orinoco river plume-influenced waters. Given the new SMOS data, the spatial and
483 temporal coherence between SSS and optical properties of the river plumes, e.g. CDOM,
484 can now be systematically analyzed.



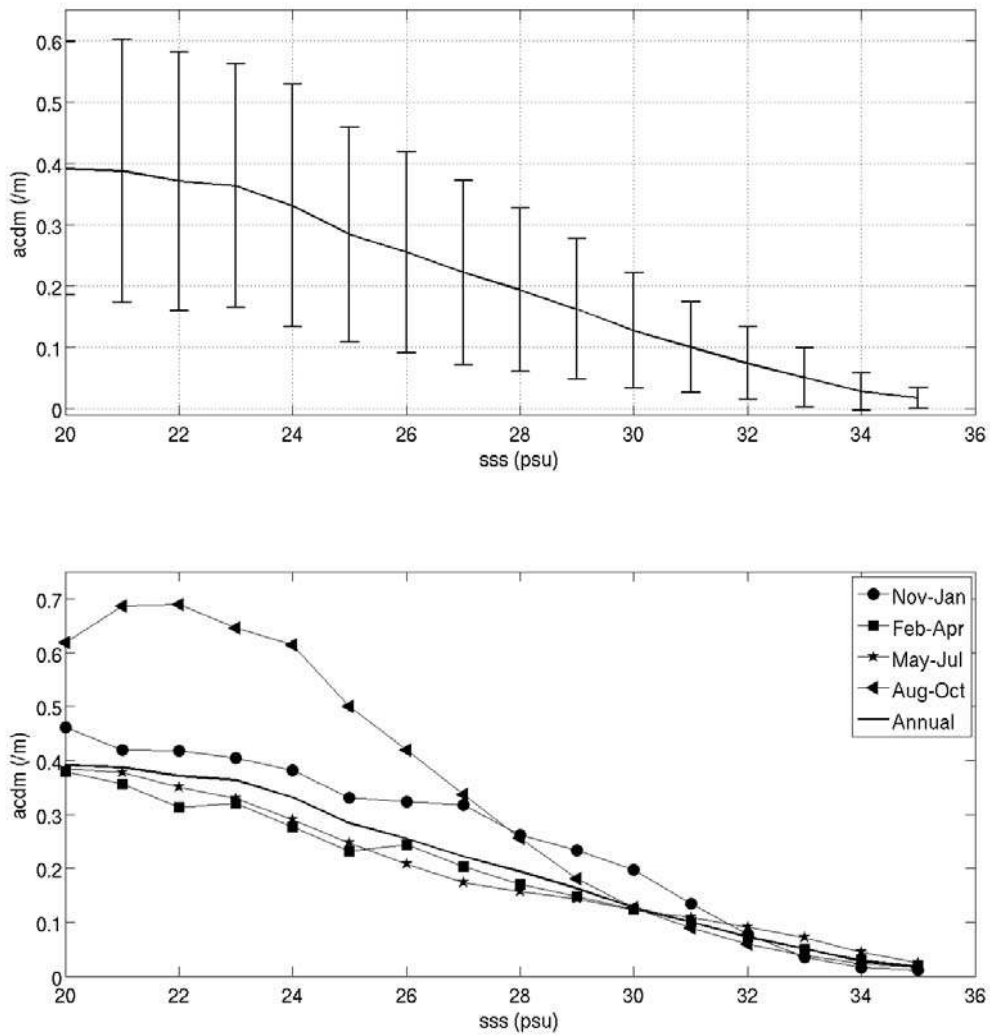
485
 486 **Figure 6:** Seasonal cycle of the freshwater Amazon and Orinoco river Plume signals for
 487 year 2010. Left: SSS from SMOS averaged over the different periods of the discharge
 488 cycle. From Top to bottom: Low Flow (Nov.-Jan.); Ascending flow (Feb.-Apr.); High-flow
 489 (May-Jul); Descending flow (Aug.-Oct). Right: corresponding CDOM absorption coefficient
 490 averaged from the merged MERIS/MODIS products. The colorbar is logarithmic in unit of
 491 $1/m$.
 492

493 As illustrated in Figure 5, the amplitude of the annual cycle of the Amazon river discharge
 494 peaks in June-July and was apparently more important in 2010 and 2011 compared to the
 495 averaged 'climatological' cycle since 1968. In comparison the discharge from Orinoco is
 496 much lower and peaks in September. Based upon the Amazon river discharge cycle, four

497 main periods can be distinguished as shown in Figure 6. From November to April (low
498 flow and ascending periods), the plume is carried northwestward with the NBC while the
499 summer and fall display a plume mostly carried eastward as the seasonal NECC
500 retroflection strengthens. In comparison, the spatial pattern in the distributions of the
501 CDOM are in general very similar to SSS during the river discharge seasonal cycle.
502 However, the CDOM patterns can deviate from the SSS patterns at large distances from
503 the mouth of the river for some period of the seasonal cycle. This is particularly evident in
504 the region around the northern Antilles and the Caribbean during the High flow season of
505 2010 (Figure 6, third panel from top) whereby high CDOM values are detected north of the
506 low salinity plume extent (contours at SSS=35.5 on the right panels) suggesting presence
507 of dissolved organic matter concentrations that are non-correlated with the Amazon river
508 plume dilution. Altogether, this demonstrates the strength in combining satellite SSS
509 observations with complementary satellite observations in order to better characterize the
510 variability of the pathway of freshwater runoff along with the corresponding mixing
511 processes at seasonal to interannual time scales.

512 Quasi-linear relationships between SMOS SSS and the MERIS/MODIS CDM absorption
513 coefficient (a_{cdm}) estimated for year 2010 are illustrated in Figure 7. a_{cdm} values were
514 averaged over SSS bins with 0.5 pss bin width. As evidenced, while CDOM mixing
515 processes seem to be conservative on average, clear departure from linearity are observed
516 below 30 pss during the Descending and Low-flow seasons. This fact potentially indicates
517 changes in the endmember values at the mouths of the rivers and tributaries and/or,
518 illustrate occurrence of non-conservative mixing processes as listed above. Thanks to the
519 new satellite observations, departure from conservative mixing and the inter-annual
520 sources of variability will be certainly more detailed in the next future.

521



522

523 **Figure 7:** $a_{CDOM}(490)$ to SMOS SSS dependence in the Western Tropical North Atlantic
 524 averaged over years 2010-2012 for all seasons of the Amazon River Discharge cycle (Top)
 525 and for each season separately (bottom). In the upper panel, the mean $a_{CDOM}(490)$ per 0.5
 526 pss bins is shown as a solid black line ± 1 standard deviation (vertical bars).

527

528

529

530 3.2 Eastern Tropical Atlantic Freshwater Pools Monitoring

531

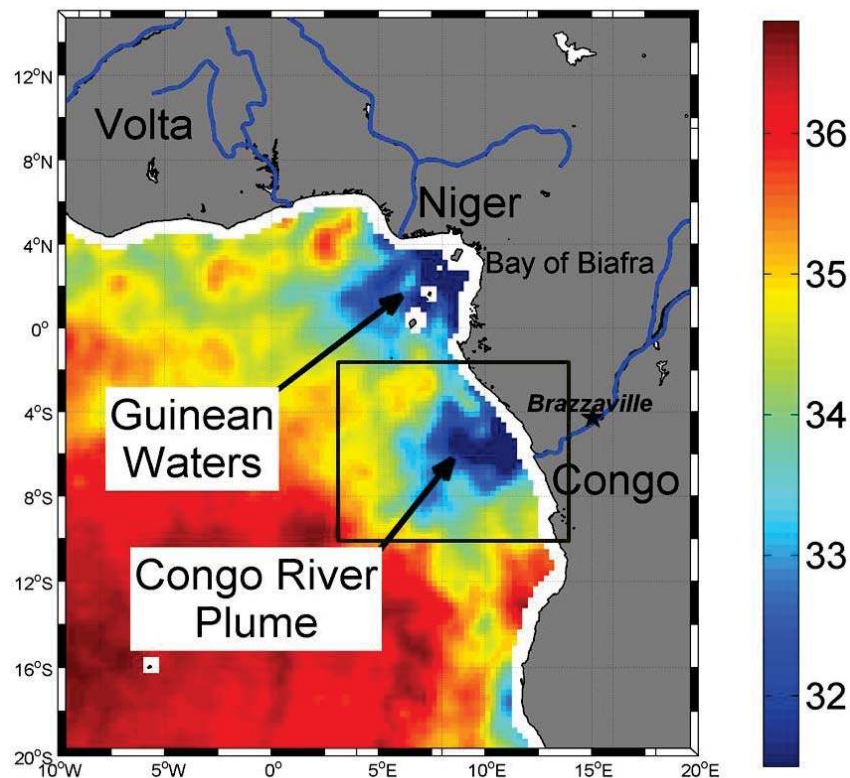
532 The Eastern Tropical Atlantic (ETA) Ocean 8°W-12°E,6°N-20°S is a region of
 533 intense upwelling and where the second largest river in the world, the Congo, enters the
 534 ocean together with the Niger, Volta and numerous other smaller rivers (Figure 8). In
 535 addition, intense precipitations also decrease SSS in the Guinea current and Northeastern
 536 Gulf of Guinea (Hisard, 1980; Merle, 1980). The ETA is therefore characterized with a

537 highly complex hydrographic system, largely influenced by the Congo River, intense
538 precipitation, and strong seasonal coastal and equatorial upwelling in the boreal summer.

539 Maximum discharge from the Congo River occurs in December and minimum
540 discharge in March through April. The outflow is hardly detectable from SST or sea level
541 data. In chlorophyll, however, the mouth of the Congo River shows a strong signal all year
542 round with large plumes extending offshore. While these ocean colour signals highlight
543 real oceanographic features of the plume, frequent cloud cover found in this region during
544 the rainy season strongly inhibits the spatio-temporal evolution of the Congo plume
545 structure to be monitored.

546

547



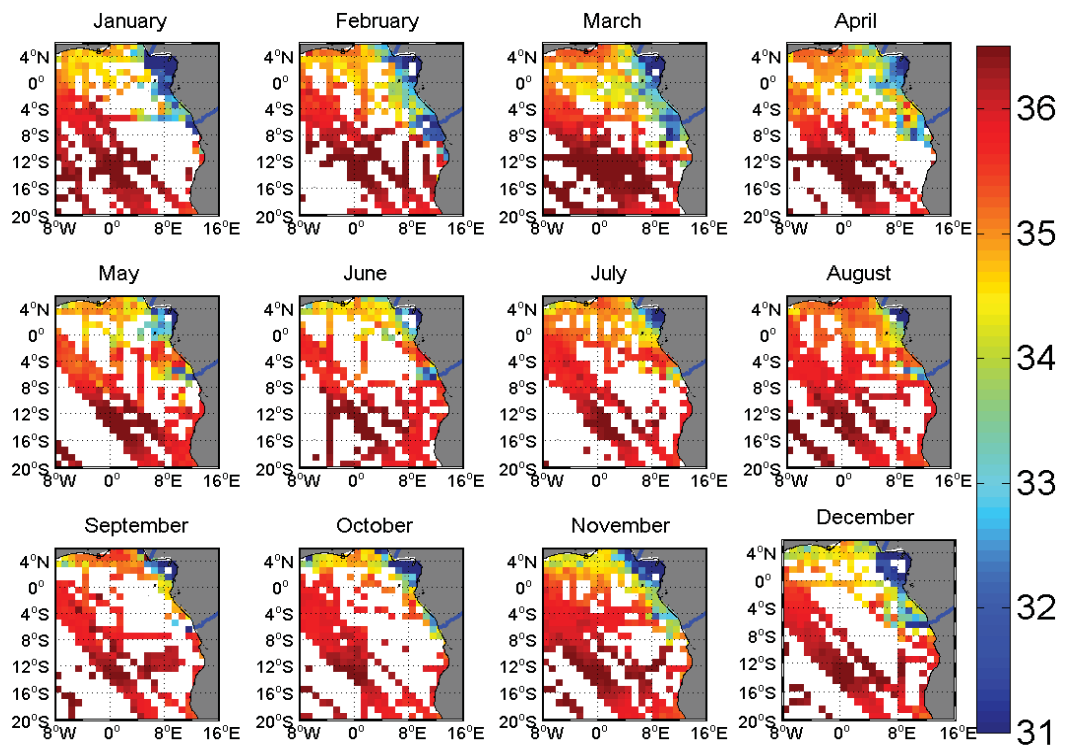
548

549 **Figure 8:** Map of SMOS SSS in the Gulf of Guinea and Southeast Atlantic Ocean
550 indicating the two largest pools of low salinity waters in the eastern tropical Atlantic: the
551 Bight of Biafra (Guinean waters) and the Congo River plume. The map was generated by
552 averaging SMOS data over 2010-2012 considering only data acquired during months of
553 April.

554

555 Hitherto the knowledge about the seasonal extension and spreading of the Congo river
556 plume is therefore mainly relying on dedicated *in situ* surveys (e.g. see Meulenbergh 1968;
557 Koleshnikov, 1973 ;Bornhold, 1973; Wauthy, 1977;van Bennekom et al., 1978; Eisma and
558 Van Bennekom, 1978; van Bennekomand Berger, 1984; Piton andWacongne, 1985; Braga

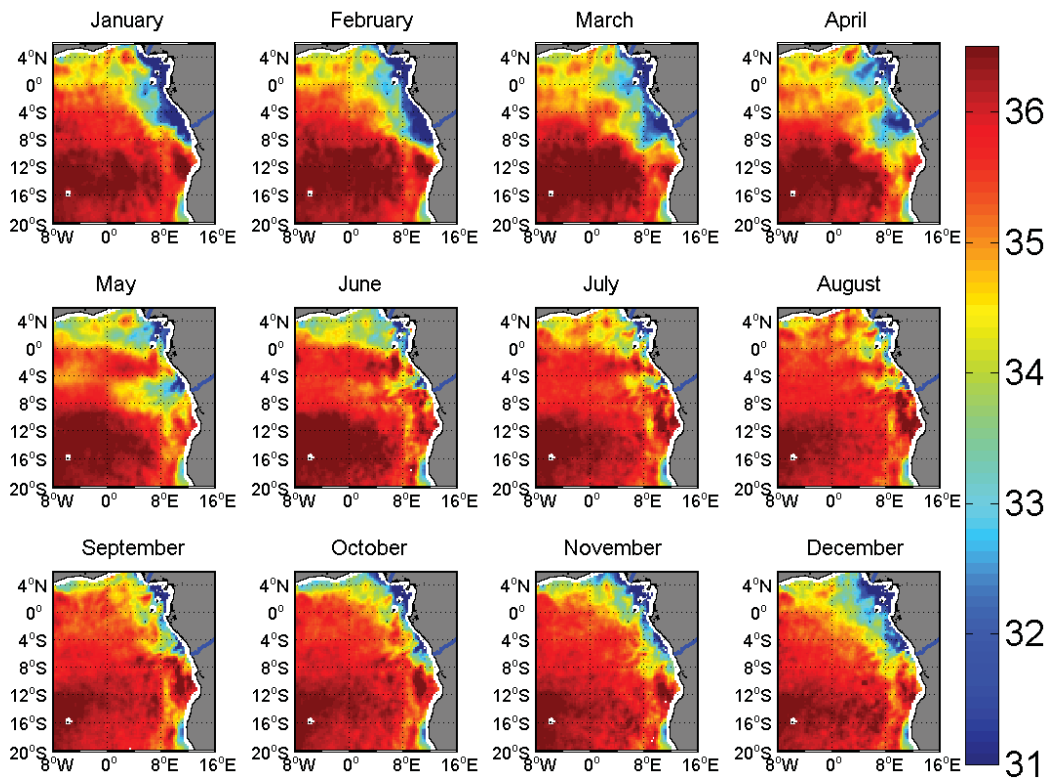
559 et al., 2004; Reverdin et al., 2007; Vangriesheim et al., 2009; Lefevre 2009). However, the
 560 ensemble of in situ SSS data collected during the period 1977–2002 in the ETA is sparse
 561 and only enabled retrievals of low-resolution ($1^\circ \times 1^\circ$) monthly climatology of the SSS field
 562 (Reverdin et al., 2007), as displayed in Figure 9. Since 2003 the *in situ* SSS sampling has
 563 improved with the increasing deployments and operations of Argo floats.
 564



565
 566 **Figure 9:** Maps of the monthly averaged SSS in the ETA derived from the ensemble of *in*
 567 *situ* measurements collected during the period 1977-2002 and used to build up Reverdin et
 568 *al.*, 2007 climatology.
 569

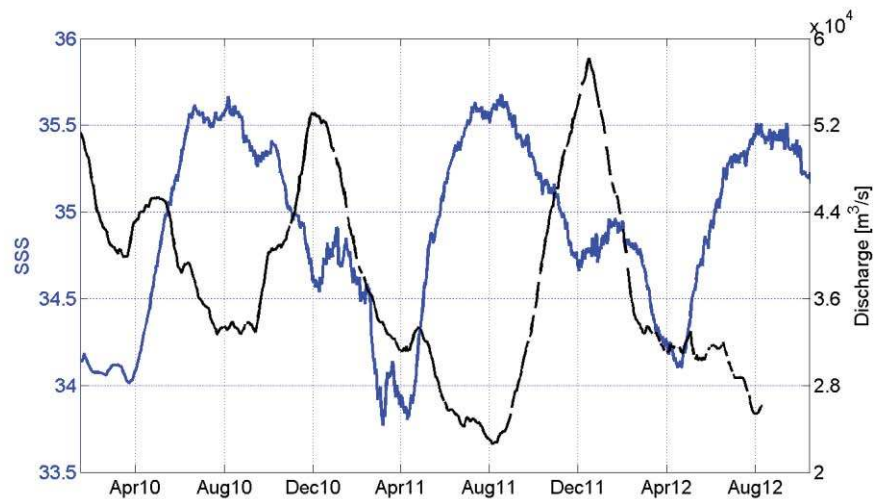
570 The monthly averaged SMOS SSS maps shown in Figure 10 were generated by combining
 571 SSS data over the SMOS 3 years life period. As evidenced in detail by these maps,
 572 consistent with historical *in situ* observations, the Congo River plume is spreading north-
 573 westward along the coast and mix with southwestward flowing freshwater from the bight
 574 of Biafra during February and March (Koleshnikov, 1973 ; Wauthy, 1977). In May (Van
 575 Bennekom et al., 1978), June-July (Bornhold, 1973; Wauthy, 1977) and August
 576 (Koleshnikov, 1973) the two fresh pools are disconnected with the Congo plume directed
 577 in westerly direction, extending up to 800-1000 km offshore, as far as 8°E. In November, a
 578 "jet stream" of low salinity water is ejected from the estuary with a large velocity and
 579 protrudes in WNW direction (Wauthy, 1977). The plume extent can also show southward

580 and south-westward legs depending on the prevailing windstress in the Angola Basin (Van
 581 Bennekom and Berger, 1984, Dessier and Donguy, 1994).



582
 583 **Figure 10:** 2010-2012 monthly averaged seasonal cycle of surface salinity in the Eastern
 584 Tropical Atlantic derived from SMOS observations.
 585

586 The dispersal patterns of the Congo River plume during all seasons can mostly be included
 587 inside the rectangle domain shown in Figure 8. The 10-day running mean time series of the
 588 SMOS SSS averaged over that spatial domain is shown in Figure 11 together with the time
 589 series of the river discharge measured at Brazaville gauge station during the period 2010-
 590 2012. Maxima in the averaged SSS within that region occur regularly in August at the time
 591 of the Congo river minimum discharge. Minima in SSS (detected around April) however
 592 lag by approximately 4 months the maxima in the river discharge at Brazaville station
 593 (found around December-January). These lags probably indicate the time for the
 594 freshwater masses to be transported from Brazaville to the river mouth and then to be
 595 further advected by surface currents far offshore. However, the inter-annual variability in
 596 the amplitude of the seasonal cycle of SSS and river discharge are not correlated. While the
 597 river discharge reached significantly different minimum values of $\sim 3.3 \times 10^4 \text{ m}^3/\text{s}$ and ~ 2.3
 598 $\times 10^4 \text{ m}^3/\text{s}$ in 2010 and 2011, respectively, the maxima in the averaged SSS is constantly
 599 found at ~ 35.5 pss. Similarly, the maximum discharge level of $\sim 5.8 \times 10^4 \text{ m}^3/\text{s}$ measured
 600 over the period is found in January 2012 while the minimum in the averaged SSS (~ 31.9)
 601 occurred in April 2011.



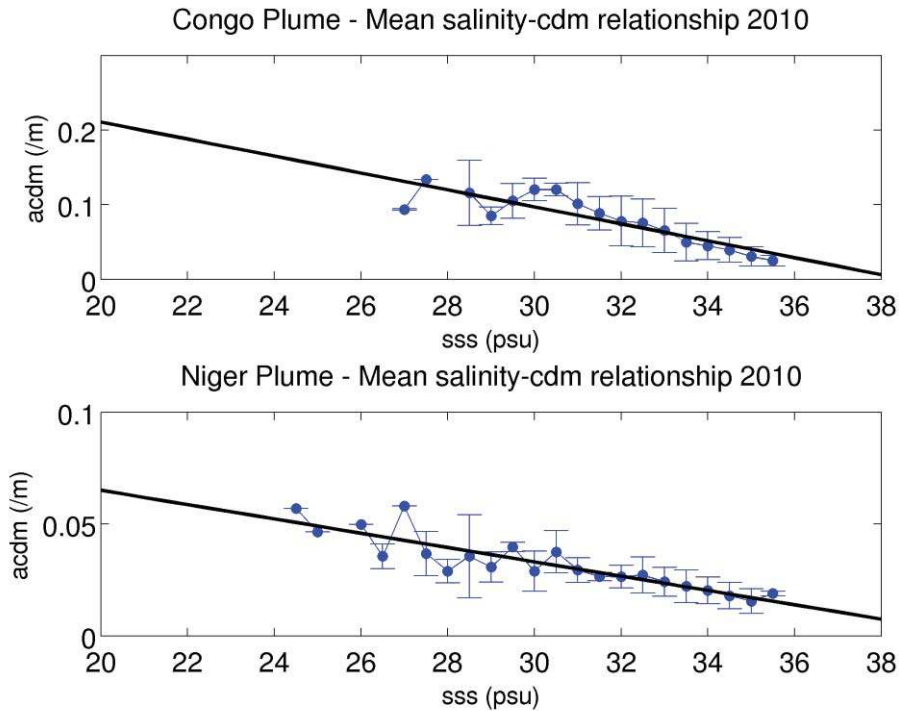
602

603 **Figure 11:** *Times series of (i) the SMOS SSS averaged over the spatial domain [3°E-*
 604 *14°E;10°S-2°S] illustrated by the black rectangle in Figure 8 (blue) and (ii) of the Congo*
 605 *discharge level measured at Brazaville (black).*

606

607 While understanding the observed satellite SSS trend in that region is still an undergoing
 608 activity, combining satellite information on surface currents, SST, rain rates and SSS
 609 together with River discharge levels will certainly help in the near future to better quantify
 610 the sources of variability in the local hydrological cycle of the Gulf of Guinea. The
 611 terrestrial and atmospheric hydrological fluxes in this region also act as a dominant
 612 modulator of the local fishery. The regular SMOS SSS data can therefore help to better
 613 understand the mechanisms involved in the biophysical interplay and its relevance for the
 614 fishery with potentially significant socio-economic impact in that region.

615 In addition, similarly to the Amazon-Orinoco river plumes, conservative mixing
 616 laws for bio-optical properties of the major river plume in the ETA region can now be
 617 systematically studied using SMOS data as shown in Figure 12. Examples of the
 618 conservative mixing linear laws for the CDOM coefficient deduced only from spaceborne
 619 measurements are shown for year 2010 around the Congo and Niger river.



620

621 **Figure 12:** $a_{CDOM}(490)$ to SMOS SSS dependence in the Eastern Tropical Atlantic
 622 averaged over year 2010 for the Congo(Top) and Niger (Bottom) River Plumes. The mean
 623 $a_{CDOM}(490)$ per 0.5psu bins is shown as a solid black line ± 1 standard deviation (vertical
 624 bars).

625

626

627 4. Precipitation signatures in SSS data from Space

628

629 Large vertical gradients can develop in the upper few meters of the ocean after a heavy
 630 rainfall, as first evidenced during the Tropical Oceans-Global Atmosphere Coupled Ocean-
 631 Atmosphere Response Experiment (TOGA COARE) (Soloviev and Lukas, 1996; Schlössel
 632 et al., 1997; Wijesekera et al. 1999). The downward fresh water flux at the sea surface
 633 establishes a haline diffusive molecular layer (or freshwater skin of the ocean) (Katsaros
 634 and Buettner, 1969) that is characterized by a salinity gradient, with salinity differences
 635 across this freshwater skin sometimes greater than 4 salinity unit. The residual effects of
 636 the rain-induced skin layers can even be stronger at the highest rain rates (Schlössel et al.,
 637 1997). This freshwater skin stabilizes the near-surface layer (Ostapoff et al., 1973) and tends
 638 to dampen free convection in the upper oceanic boundary layer.

639 These conditions motivate the development of autonomous sea surface salinity drifters able
 640 to monitor the salinity at less than 50 cm depth. Using such instruments, Reverdin et al.,
 641 (2012) documented salinity freshening between 15 cm and 50 cm depth in the tropical

642 oceans. Sudden salinity decreases are often associated with local rainfall and vertical
643 salinity gradients that last for a few hour, depending, among other factors, on wind speed
644 conditions. The haline molecular diffusion layer that is established in the upper ocean
645 during rainfall can thus be important for the radiometric observation of the sea-surface at
646 low microwave frequencies. At centimeter wavelengths the dielectric constant is modified
647 by the sea-surface salinity (e. g. Klein and Swift, 1977; Yueh et al., 2001) and any change
648 of the latter might cause interpretation problems when comparing remotely measured
649 surface salinity at these frequencies to deeper *in situ* measurements.

650 Hence, under rainy conditions (or just after a rainfall), satellite SSS shall better
651 characterize the salinity at the ocean-atmosphere interface rather than the 1-10 m deep *in*
652 *situ* samples. Whether accumulated precipitation can be estimated from changes in salinity
653 at the ocean surface as observed from Space remains however an open question, as
654 assumptions have to be made about the penetration depth of the fresh water. In addition,
655 assimilation of the new satellite SSS data into ocean circulation models having limited
656 vertical resolution also challenges our modeling perspectives concerning the dynamics of
657 the first centimeters to first meter of the ocean surface.

658

659 In the following section, we discuss signatures of precipitation detected in the new SMOS
660 SSS data. First, the strong SSS spatio-temporal variability associated with rain events as
661 seen both by spaceborne and *in situ* sensors in the Pacific Ocean Inter-Tropical
662 convergence zone is presented. Second, it is revealed that the SSS from space is
663 systematically showing lower values (negative bias) with respect to the deeper 5-10 m
664 depth of Argo upper salinity. These effects are shown to be statistically correlated with
665 rain. Third, long-lived, large-area and large amplitude SMOS SSS anomaly patterns in the
666 Tropical Atlantic are shown to follow local anomaly patterns in the Evaporation-
667 Precipitation (E-P) budget. Finally, the preliminary results of the inter-annual variability
668 of the SMOS SSS signal in the Indian and in the Tropical Pacific oceans and connections
669 to key climate indexes will be presented and discussed.

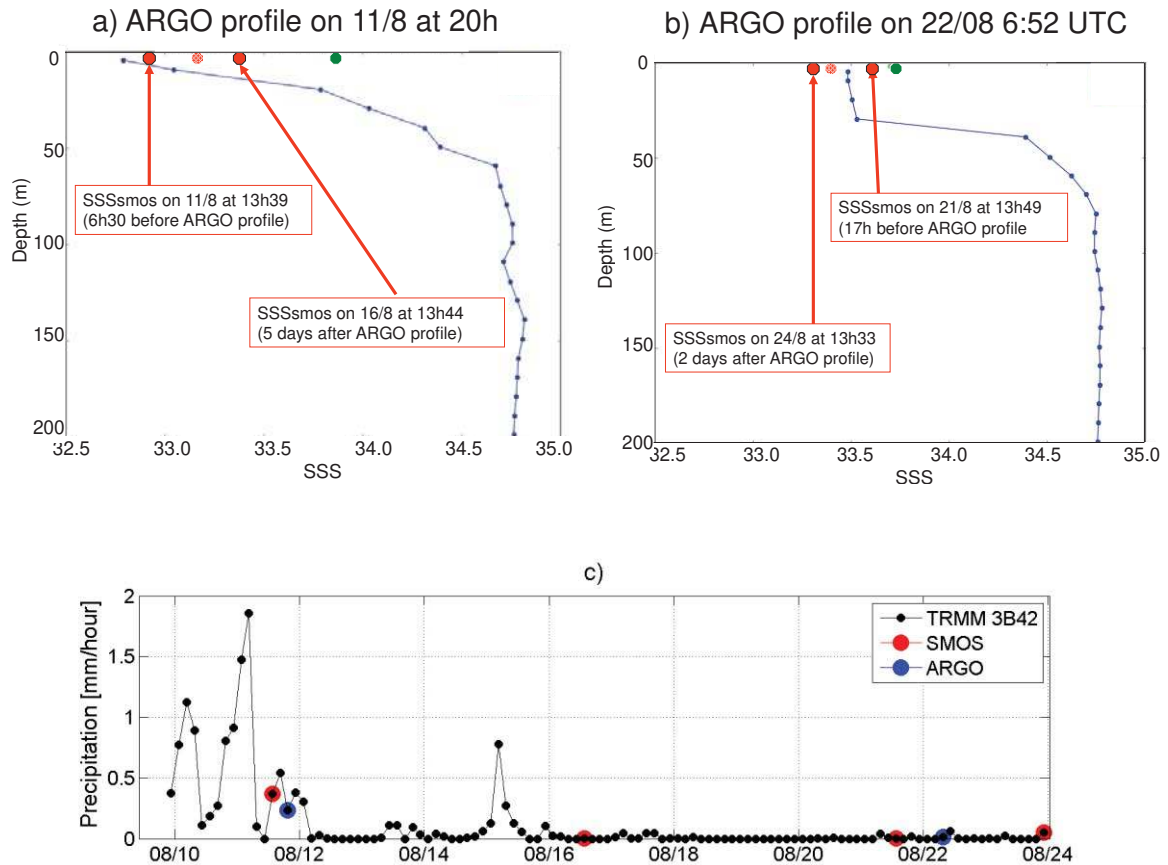
670

671 **4.1 SSS temporal variability associated with rain events**

672

673 Although satellite observations provide a better sampling of the global ocean than the *in*
674 *situ* observing systems, such as the Argo float array, individual SSS measurements are
675 obtained in rainy regions with a strong temporal variability seen on both SMOS and Argo

676 SSS. In Figure 13, we show such an example of co-located SMOS and Argo profiler
 677 measurements in the InterTropical Convergence Zone of the Tropical Pacific indicating a
 678 significant surface freshening associated with a rain event. On 11 August 2010, the Argo
 679 float WMO id#4900325 detected a freshening of 0.9 between 20 m and 5.5 m depth
 680 (Figure. 13a). In contrast, the Argo profile derived on 22 August shows that the salinity
 681 between 30m and 5m depth is much more homogeneous with more saline water at 5m
 682 depth compared to the one recorded on 11 August.



683
 684
 685 **Figure 13:** Two successive Argo profiles taken by float 4900325 (blue curve) in the Eastern
 686 Tropical Pacific on (a) 11 August 20:00 UTC (latitude=12.4°N; longitude=117.6°W) and
 687 (b) 22 August 6:52 UTC (latitude:12.2° N; longitude: 117.8° W). Mean SMOS SSS
 688 collocated within a 5 days window and a radii of 50 km with these profiles are indicated
 689 by red dashed point. In each case, two SMOS passes have participated to these
 690 collocations: mean SMOS SSS corresponding to each pass is indicated as red filled point.
 691 The corresponding ISAS SSS in August is indicated by the green point. The time series of
 692 the 3-hourly satellite rain rate from TRMM 3B42 and averaged over [11°N-13°N; 116°W-
 693 118°W] is provided in c). The time at which SMOS and Argo acquired SSS data is
 694 indicated by red and blue dots, respectively.

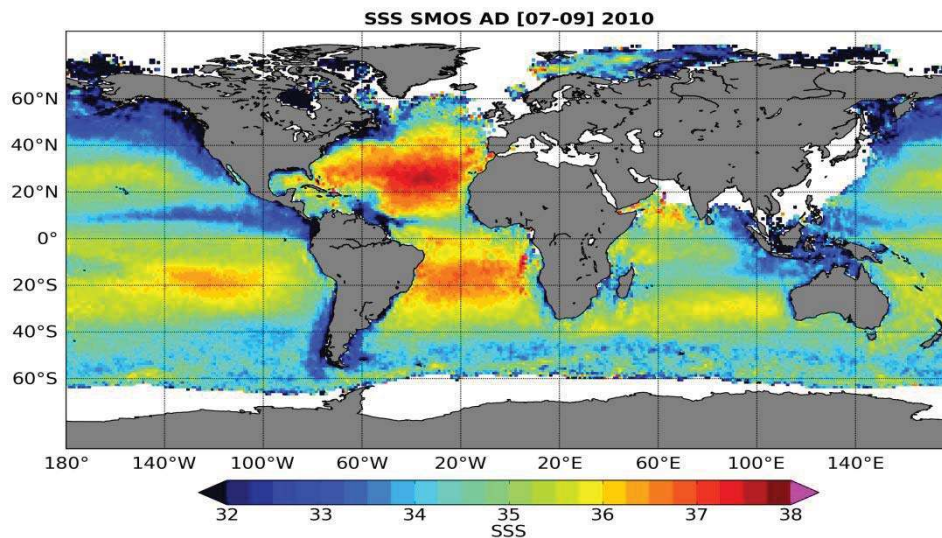
695
 696 The TRMM satellite Rain-Rate (RR) estimates averaged over a 2°x2° box centered on the
 697 Argo float location indicate a significant rain rate of 1-2 mm h⁻¹ on 11 August that lasted
 698 for at least a day before the Argo profile raised to the surface (Figure 13c). Contrarily,

699 negligible precipitation occurred on 22 August and during the preceding week. The first
700 SMOS pass collocated with the 11 August Argo profile (Figure 13a) was acquired also
701 during rainy conditions and is showing a low SSS of ~32.8 (0.1 saltier than the Argo SSS
702 taken 6:30 h later, Figure 13c). The second SMOS pass on the 16th August occurred under
703 non-rainy condition (Figure 13c) and is 0.5 saltier. Consistent with the 22 August Argo
704 profile (Figure 13b) observations, the collocated SMOS SSS during these rain-free
705 conditions (Figure 13c) are also significantly saltier by 0.4-0.6. The large SSS variation
706 (0.7) measured by this Argo float at a 10 day interval and by the collocated SMOS
707 measurements over several SMOS passes clearly demonstrates the influence of the rain
708 timing on the SMOS-Argo SSS differences.

709

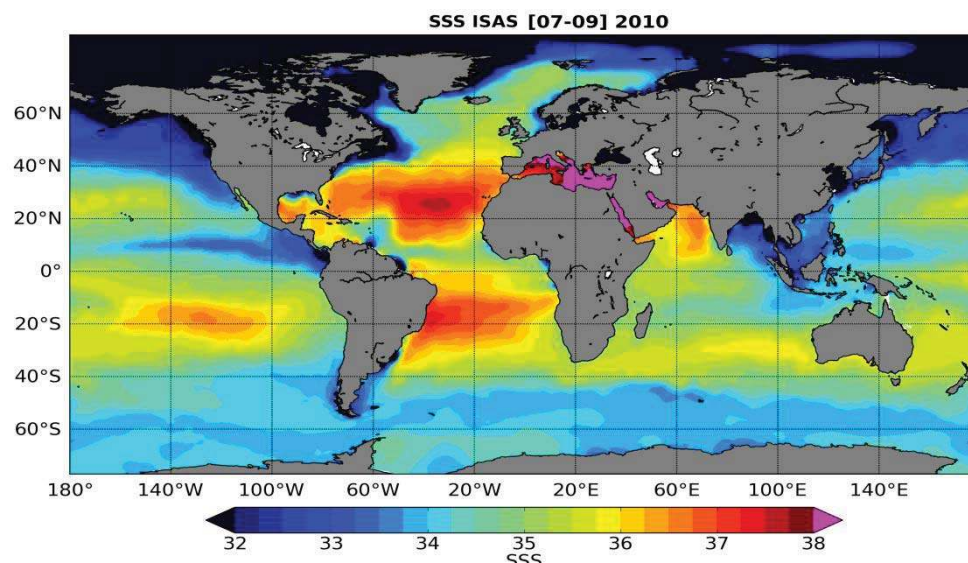
710 4.2 Systematically fresher skin SSS in rainy regions

711



712

713



714 **Figure 14:** Maps of SSS averaged from July to September 2010, derived from (top) SMOS
 715 ascending and descending orbits and ISAS (bottom).
 716

717 The SMOS SSS map averaged over July–September 2010 is compared to Optimally
 718 Interpolated *in situ* ISAS map averaged over the same period on Figure 14. At large scale,
 719 SSS spatial variability sensed by SMOS is consistent with ISAS. A striking visual feature
 720 of the SMOS SSS map compared to the *ISAS map* in the tropics is the freshest SSS in the
 721 North Tropical Pacific, under the location of the ITCZ (particularly west of 120°W).

	Mean (Δ SSS)	Std (Δ SSS)	<i>N</i>
Subtropical Atlantic Ocean (15°N–30°N; 45°W–30°W)	−0.13	0.28	206
Tropical Pacific Ocean (5°N–15°N; 180°W–110°W)	−0.23	0.35	692
Southern Indian Ocean (40°S–30°S; 70°E–90°E)	0.04	0.39	114
Southern Pacific Ocean (50°S–40°S; 180°W–100°W)	−0.08	0.51	467

722

723 **Table 2.** Comparison of SMOS SSS (10day, 100×100 km² average) collocated with Argo
 724 upper depth measurements. Δ SSS=SSS_{smos}−SSS_{argo} Only SMOS ascending orbits are
 725 considered. Std (Δ SSS) primarily reflects the decreasing signal to noise ratio with
 726 decreasing SST. Note that subtropical Atlantic Ocean and tropical Pacific Ocean have
 727 similar SST.
 728

729 When SMOS SSS are precisely collocated around Argo SSS in various regions of the
 730 global ocean (see Boutin et al. (2012)), a more negative bias (~-0.1 than in other regions)
 731 and larger standard deviation are systematically observed between 5°N and 15°N in the
 732 Pacific Ocean with respect to other regions (Table 2).

733 To investigate if a systematic negative bias of ~-0.1 between the satellite skin depth SSS
 734 and the ~5 m depth Argo floats data could be related to rain-induced vertical stratification,
 735 a triple collocation between Argo, SMOS Level 2 products (at ~40 km resolution, non
 736 averaged in time) and SSMI satellite rain rate (RR) data was conducted. SMOS and SSMI
 737 RR data were co-located within a temporal window of −40min and +80 min while a +/-
 738 5days windows was considered to co-locate SMOS and Argo data.

739 The theoretical error on the SMOS SSS retrieved Level 2 data used in this
 740 collocation exercise is ~ 0.5. Without any RR sorting, the statistical distribution of the

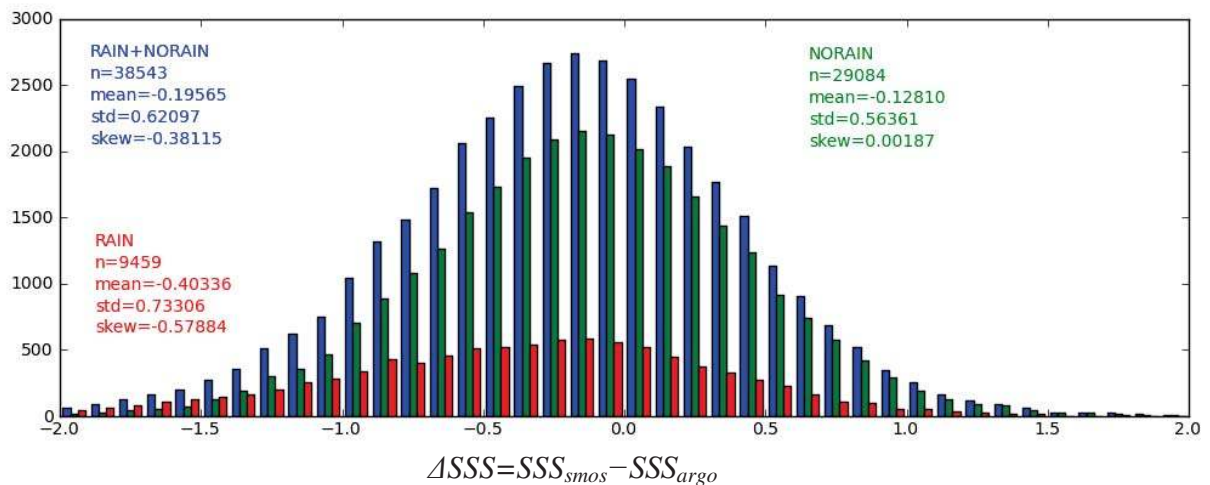
741 differences ΔSSS is skewed towards negative values (Figure 15 and Table 3); when only
 742 SMOS non rainy events are considered, the negative skewness disappears, and statistics of
 743 the SMOS-Argo differences in the Tropical Pacific Ocean become close to the ones in the
 744 subtropical Atlantic Ocean (Tables 2 and 3). Largest skewness towards negatives
 745 differences are obtained when only SMOS SSS close to rain events are considered. For
 746 these rainy SMOS cases, we find a negative dependency of the SMOS-Argo SSS
 747 differences with respect to SSM/I RR of $-0.17 \text{ pss/mm}^{-1} \text{ h}$, i.e., a freshening of 1.7 for a
 748 SSM/I RR of 10 mmh^{-1} (Boutin et al., 2012).
 749

	Mean(ΔSSS)	Std(ΔSSS)	Skew(ΔSSS)	N
Tropical Pacific (5°N-15°N; 110°W; 180°W)				
All collocations	-0.20	0.62	-0.38	38543
No Rain (RR < 0.1 mm hr ⁻¹)	-0.13	0.56	0.01	29084
Rainy (RR ≥ 0.1 mm hr ⁻¹)	-0.40	0.73	-0.58	9459

750

751 **Table 3:** Statistics for the SSS differences $\Delta SSS = SSS_{smos} - SSS_{argo}$ as a function of Rain Rate
 752 (RR) in the Northern Tropical Pacific Ocean
 753

754



755
756

757 **Figure 15:** Statistical distribution of SSS differences $\Delta SSS = SSS_{smos} - SSS_{argo}$ in the Tropical
 758 Pacific Ocean for various sorting on co-located SSM/I rain rates. Blue: all collocations
 759 (without any rain sorting); green: for non rainy cases (SSM/I rain rates less than 0.1 mmh^{-1});
 760 red: rainy cases (SSM/I rain rates larger than 0.1 mmh^{-1}). Corresponding statistics are
 761 indicated in Table 3.
 762

763 The non sorting of SMOS measurements close in time with rain events in SMOS-Argo
 764 collocated datasets (within 10 days and 100 km) is responsible for (i) a mean -0.1 negative

765 bias over 3 months between 5° N and 15°N in the Tropical Pacific region with respect to
 766 non rainy conditions and with respect to the subtropical Atlantic region, and (ii) a negative
 767 skewness of the statistical distribution of SMOS minus Argo SSS difference (Figure 15).
 768 Given that the whole set of SMOS-Argo collocations also includes the situations with rainy
 769 Argo measurements collocated with non rainy SMOS measurements, these results indicate
 770 a systematic freshening of SMOS SSS in rainy conditions and is likely a signature of the
 771 vertical salinity stratification between the first centimeter of the sea surface layer sampled
 772 by SMOS and the 5m depth sampled by Argo. For more detail on the vertical SSS
 773 stratification induced by rain, the reader is also referred to Boutin et al. (2012b).

774

775 **4.3 SSS as a tracer of the Evaporation-Precipitation budget in the oceanic mixed layer**

776

777 The SMOS derived SSS can also be used to investigate the consistency between
 778 observed SSS variability and the Evaporation minus Precipitation budget in the ITCZ of
 779 the tropical Atlantic based upon the SSS and SST relationship in the ocean mixed layer
 780 (OML). The salt conservation budget in the OML with depth h can be expressed as follows
 781 (Michel, 2007; Yu 2010, 2011):

782

$$783 \frac{\partial S}{\partial t} = \frac{(E - P - R)S}{h} - \vec{u} \cdot \nabla S - \Gamma(w_e) \frac{w_e(S - S_h)}{h} + \kappa \nabla^2 S \quad (1)$$

784

785 where S is the surface salinity, E and P , the evaporation and precipitation rates,
 786 respectively, R the fresh water input by river runoffs, h , the mixed layer depth, \vec{u} the
 787 (vertically averaged) current vector within the OML and w_e , the vertical entrainment rate.

788 S_h is the salinity just below the OML, κ is the horizontal diffusivity coefficient ($\kappa \sim 2000$

789 $\text{m}\cdot\text{s}^{-2}$). The total entrainment term must be treated differently in case of upward or

790 downward entrainment, so it is multiplied by a step function Γ in Eq (1). Indeed, when

791 additional water is included into the mixed layer, its properties are affected by mixing with

792 the deeper layer: $\Gamma(w_e) = we$ if $we > 0$. On the contrary, if water is removed from the mixed

793 layer, the properties of the remaining water are conserved and only its depth h can change:

794 $\Gamma(w_e) = 0$ if $we < 0$. The vertical processes are conveniently represented by a single

795 entrainment term, consisting of the vertical Ekman advection and the OML conditions.

796 The first term in the right-hand side of Eq. (1) is the net fresh water flux. The impact of
 797 this flux on the surface water strongly depends on the salinity itself. Moreover, SSS has no
 798 direct feedback on the surface flux. These particularities have important consequences on
 799 the salt budget and on the duration of SSS anomalies. The second term is the horizontal
 800 advection of salinity by surface currents that can be separated into a wind induced
 801 component, the Ekman transport, and the geostrophic current. Ekman transport is due to
 802 wind friction on the sea surface, which is rotated by the Coriolis force as it penetrates in
 803 depth. The Ekman layer depth is systematically lower than the mixed layer depth, because
 804 both increases with the wind stress, although the depth of the mixed layer also deepens in
 805 response to other processes. Thus, the Ekman transport occurs entirely in the OML. In
 806 addition, the geostrophic current that arise from the balance between the horizontal
 807 pressure force and the Coriolis force can usually be considered constant the mixed layer
 808 resulting from the homogeneous density structure.

809 The value of the SMOS SSS at a fixed point, $S(t,r)$, is obtained by averaging individual
 810 SMOS swath SSS measurements over a considerable time interval $(t-\tau/2, t+\tau/2)$, say 10
 811 days, which is enough to filter out noise in the SSS. Suppose that the climate mean, or
 812 norm, of this SSS (provided by climatology) is $\overline{S(t,r)} = S_o(t,r)$. In the following, we
 813 define the SSS anomaly as the departure of the SSS from the norm:

$$\Delta S(t,r) = S(t,r) - S_o(t,r)$$

814
 815 Following approaches traditionally used for studying large-area SST anomalies (Piterbarg,
 816 and Ostrovskii, 1997), a formal definition can be introduced for the large-area SSS
 817 anomalies. For example, large area and large amplitude SSS anomaly comprises the
 818 connected components of the set:

$$\{(x,y): |\Delta S(t,r)| > S_T\}$$

819
 820 where $r=(x,y)$ and S_T is a threshold that can be taken either as a fixed salinity value, for
 821 example, 0.2 pss, or as a function of the standard deviation of SSS anomalies, σ_S , for
 822 example $0.5 \sigma_S$. This choice for the threshold depends on the magnitude of the anomaly of
 823 interest.

824 In the tropical Atlantic, Michel et al. (2007) and Yu (2011) have shown that the dominant
 825 terms of the mixed-layer salinity balance are horizontal advection by Ekman and
 826 geostrophic currents and the atmospheric forcing fluxes (E-P-R). In that context, the
 827 salinity balance equation in the OML can be simplified as follows:

$$\frac{\partial S}{\partial t} \cong \frac{(E - P - R)S}{h} - \vec{u} \cdot \nabla S \quad (\text{Eq. 2})$$

828

829 Using OSCAR surface current products (which comprise contributions of both Ekman and
830 geostrophic currents), the horizontal salt advection term $\vec{u} \cdot \nabla S$ can be deduced from

831 SMOS observations. The following residual SSS anomaly can then be estimated from
832 SMOS temporal observations of salinity $S(t, r)$ at point r following:

$$\Delta S(t, r) = S(t, r) - S_o(t, r) - \vec{u}(t, r) \cdot \nabla S(t, r) \quad (\text{Eq. 3})$$

833

834 According to the simplified salinity balance (Eq. 2), *a priori* valid for the tropical Atlantic,
835 the resulting SSS anomaly given by Eq.3 shall be strongly correlated with the net fresh-
836 water flux forcing term. Examples for such SSS anomaly analysis is shown in Figure 16
837 for a selected point in the middle of the North Tropical Atlantic (16°N-35°W). From
838 TRMM precipitation and OAFLEX daily evaporation fluxes, large-area P and E anomalies
839 were also evaluated:

$$\Delta P(t, r) = P(t, r) - P_o(t, r)$$

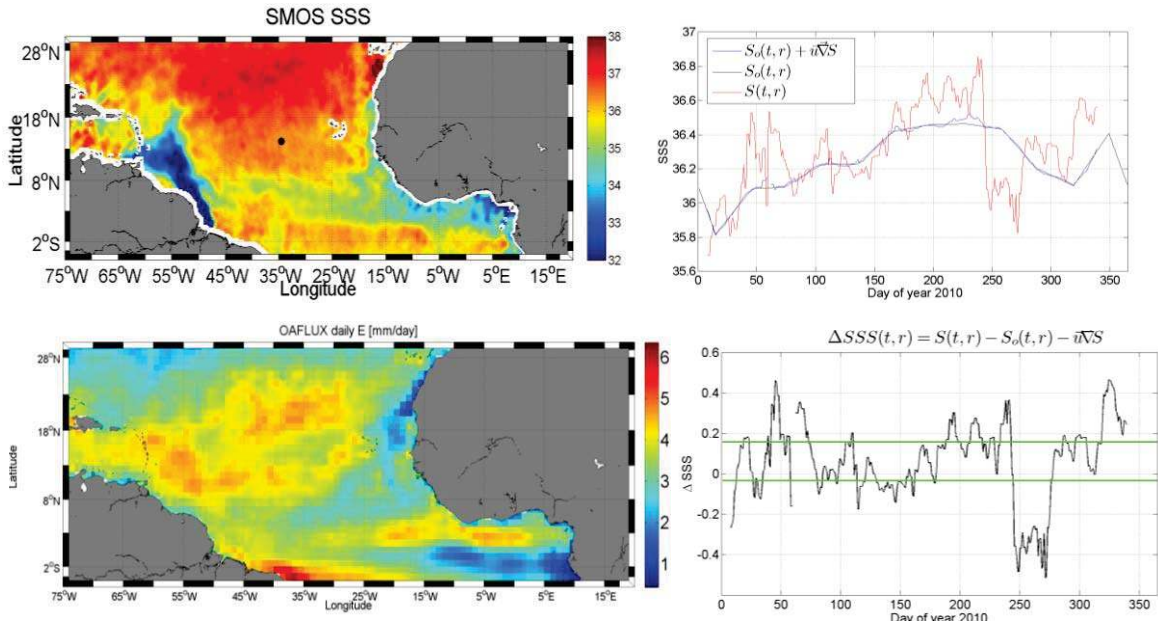
840

$$\Delta E(t, r) = E(t, r) - E_o(t, r)$$

841

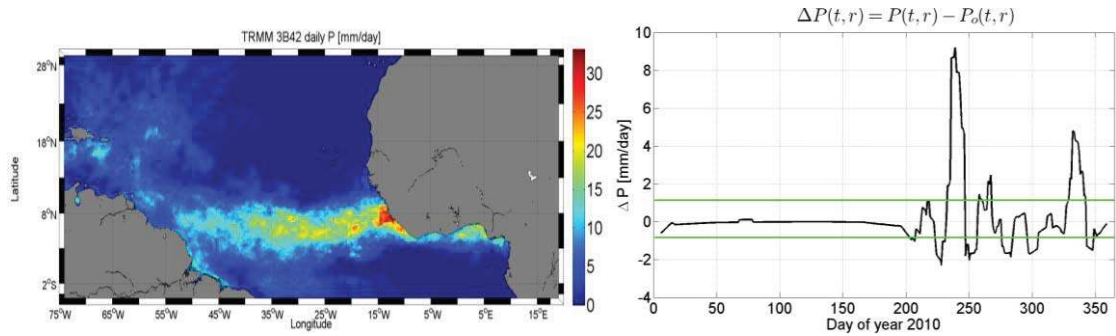
842 where P_o and E_o are the local climate mean for the precipitation and evaporation.

843



844

845



846

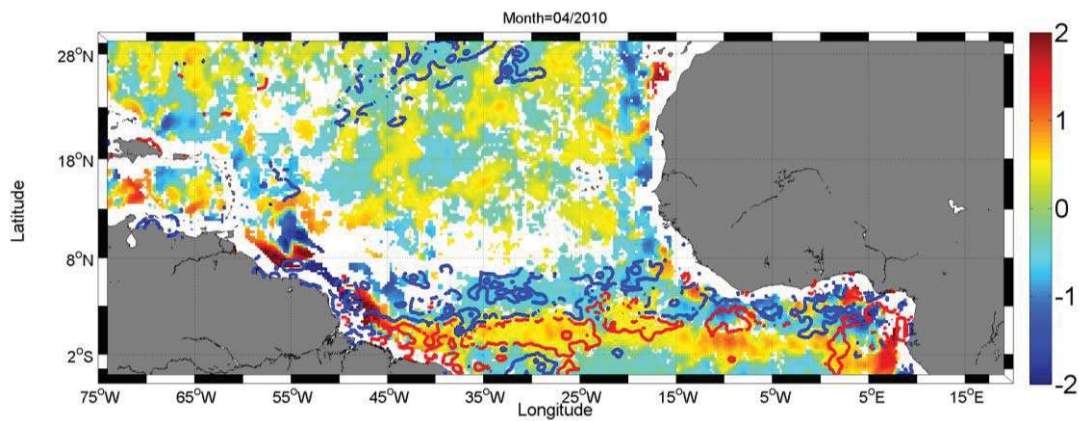
847

848 **Figure 16:** *Top left: SMOS 10-days SSS field in June 2010. Top right: time series of the*
 849 *surface salinity $S(t)$ at the black point shown in the top left figure ($35^{\circ}\text{W};16^{\circ}\text{N}$). Red:*
 850 *SMOS SSS, blue curve: local mean climatological annual cycle at that point $S_o(t)$. The*
 851 *resulting time series for the SMOS anomaly ΔSSS at that point is shown in the middle*
 852 *panel, right plot. The green horizontal lines are indicating \pm one standard deviation of the*
 853 *local SSS anomalies, σ_S . In the middle and bottom left panels, we show the corresponding*
 854 *OAF flux Evaporation and TRMM 3B42 precipitation field (mm/day). The time series of the*
 855 *Precipitation anomaly at the point is shown in the bottom right panel.*

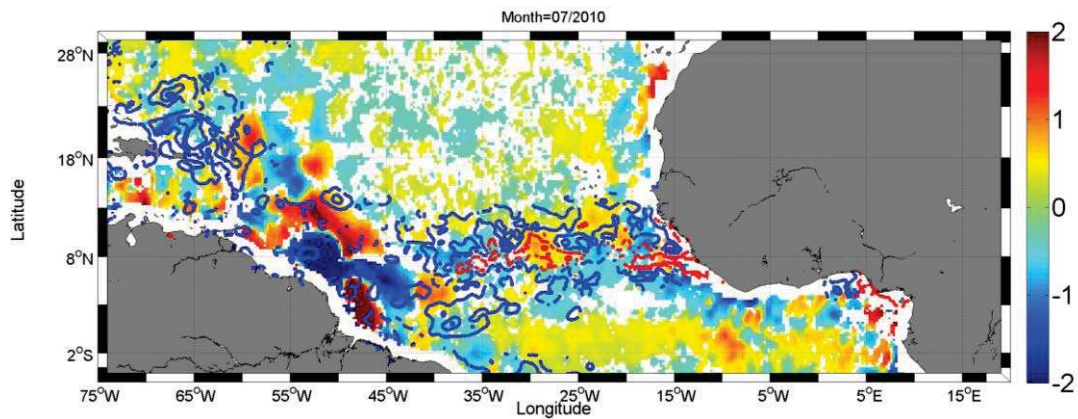
856

857 As illustrated in Figure 16 (middle right panel), very significant long-lived negative
 858 $\Delta S(t,r)$ values are detected in SMOS anomalies at the selected point in the North Tropical
 859 Atlantic during September/October months (days 250-300) of 2010. Apparently, this
 860 happened just after a strong positive anomaly in the precipitation rate as detected from
 861 TRMM during the passage of the ITCZ in August (bottom right panel).

862



863



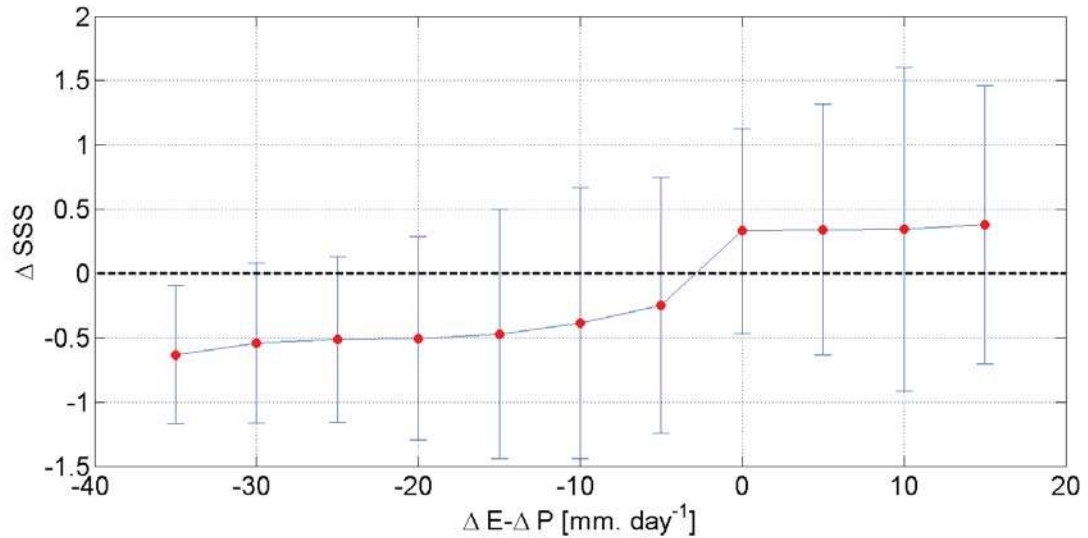
864

865 **Figure 17:** Maps of the monthly averaged large amplitude SSS anomalies deduced from
 866 SMOS data for two selected months of 2010 (Top: month of march 2010; Bottom: month
 867 of July 2010). The threshold value S_T used to derive the anomaly is defined by $1 \sigma_S$, the
 868 local standard deviation of SMOS anomaly. Superimposed are the contours of the large
 869 positive amplitude Precipitation anomalies (blue) and positive Evaporation anomalies
 870 (red).

871

872 The spatio-temporal consistency between the large area and large amplitude S, P and E
 873 anomalies can be further analyzed over all the Tropical Atlantic. This is illustrated in
 874 Figure 17 for two selected months of 2010. The spatial distribution of the large-area and
 875 long-lived (monthly averaged) SSS anomalies generally matches well the spatial patterns
 876 for the large E-P anomalies. In particular, North-South oscillation in $\Delta S(t,r)$ around the
 877 ITCZ (centered around $5^\circ N$ in March and $8^\circ N$ in July) follows the $\Delta E - \Delta P(t,r)$ far from the
 878 Amazon plume area, with negative $\Delta S(r,t)$ corresponding to positive $\Delta P(t,r)$ and positive
 879 $\Delta S(r,t)$ found in region of positive $\Delta E(t,r)$. The average relationship between SMOS SSS
 880 anomalies and the corresponding anomalies in the net atmospheric fresh water flux in the
 881 tropical Atlantic (defined here by $5^\circ S - 20^\circ N; 75^\circ W - 15^\circ E$) was further evaluated over year
 882 2010 by binning $\Delta S(t,r)$ values as function of $\Delta E - \Delta P(t,r)$ as shown in Figure 18.

883



884

885 **Figure 18:** Average relationship between SMOS SSS anomalies and the net atmospheric
 886 fresh water flux anomalies $\Delta E - \Delta P$ in the tropical Atlantic (defined here by 5°S-
 887 20°N; 75°W-15°E) over year 2010.

888

889 Despite a significant scatter in the data, the results clearly indicate the strong coherency
 890 between SMOS SSS anomalies and the Evaporation minus Precipitation flux signal in the
 891 tropical Atlantic. On average, SMOS SSS are thus systematically fresher than the SSS
 892 climatology when Precipitation rate exceed Evaporation rate with respect climatological
 893 means, and vice-versa. As expected by the skin layer effects (Zhang et al. 2012), satellite
 894 SSS anomalies are weakly sensitive to excess evaporation showing an almost constant
 895 value whatever positive values for $\Delta E - \Delta P$. Nevertheless, and as discussed in section 4, the
 896 average 0.3 salinity unit excess amplitude found for ΔS in evaporative zones is
 897 significantly larger than the expected evaporation-induced effect on the satellite SSS
 898 (~ 0.01). The source for such observed signal amplitude is not yet understood. Other
 899 physical processes, not yet well accounted for in the SSS retrieval algorithm may
 900 systematically affect the L-band brightness temperature in strongly evaporative zone (e.g.
 901 skin effects in SST, badly accounted for roughness effects at low winds).

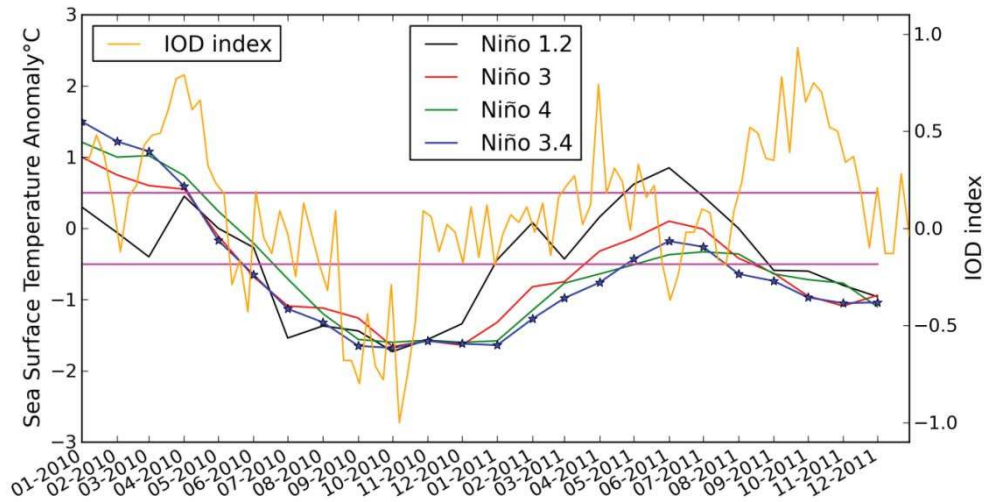
902 Nevertheless, Figure 18 clearly evidences that SSS anomalies become increasingly
 903 negative as the precipitation anomalies progressively exceed the Evaporation anomalies.

904 This shows that it is important to monitor SSS from Space in the rainy regions as it makes
 905 a good oceanic rain gauge for the changing water cycle [Cravatte et al., 2009; Yu, 2011,
 906 Terray et al., 2011], and therefore help to maintain a continuous observation network in
 907 these key regions of the marine branch of the global hydrological cycle. In that context,
 908 SMOS SSS may therefore be an interesting dataset for assimilation into ocean models in
 909 the perspective of better constraining oceanic precipitation forcing terms.

910

911 4.4 Large scale SSS inter-annual variability in tropical Indian and Pacific Oceans

912



913

Figure

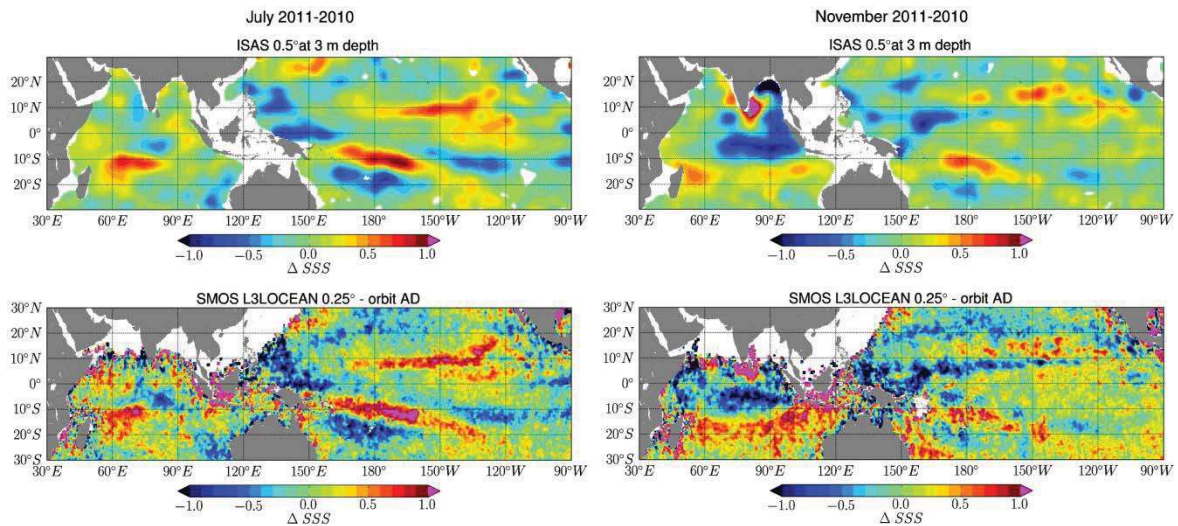
914 **19:** Time series of SST anomalies in the four Niño regions from
915 <http://www.cpc.ncep.noaa.gov/data/indices/sstoi.indices> in 2010-2011 and corresponding
916 Indian Ocean Dipole (IOD) Index (SST difference between eastern and western equatorial
917 Indian Ocean) from the Australian bureau of Meteorology (BOM).

918

919 In the Indian and Pacific Oceans the precipitation impact on the large scale SSS variability
920 can also be observed from SMOS and ISAS monthly maps.

921 The 2010-2011 period was characterized by a strong La Niña event lasting from July 2010
922 to March 2011 and by an Indian Ocean Dipole (IOD) index in negative phase in
923 September-November 2010 and in positive phase during about the same months in 2011
924 (see Figure 19). Such events are known to generate large scale SSS signatures in the
925 tropics (e.g., Gouriou et al., 2002; Singh et al. 2011, Grunseich et al. 2011) and are clearly
926 depicted in the SSS signals in both the ISAS and the SMOS monthly difference maps
927 between 2010 and 2011 for both July and November (Figure 20).

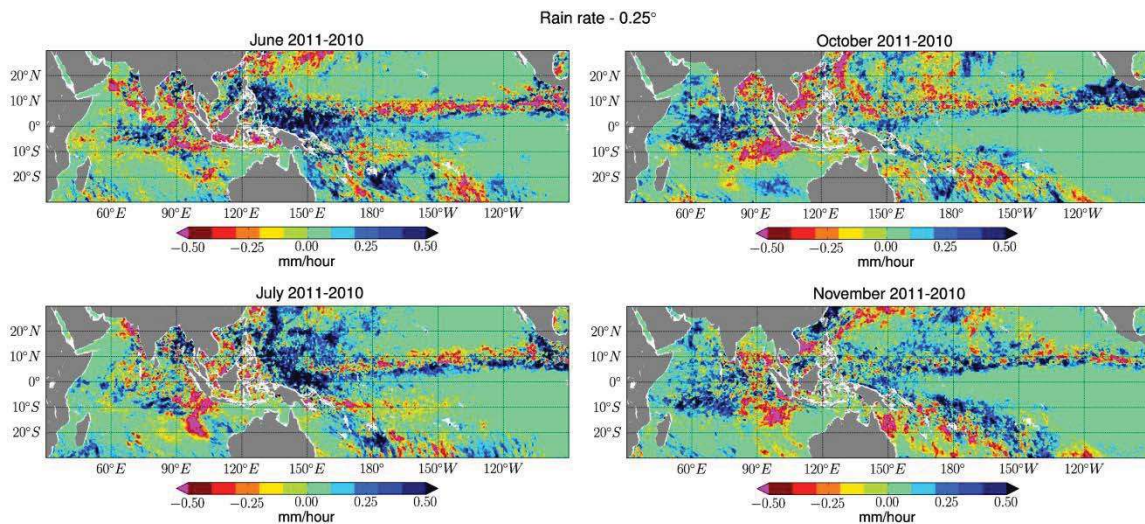
928



929

930 **Figure 20**: Differences in the monthly averaged SSS between year 2011 and 2010 for
 931 months of July (left) and November (right). Top panels show the $\Delta SSS = SSS_{2011} - SSS_{2010}$
 932 results obtained from in situ OI analysis products ISAS and bottom ones from SMOS data.
 933

934



935

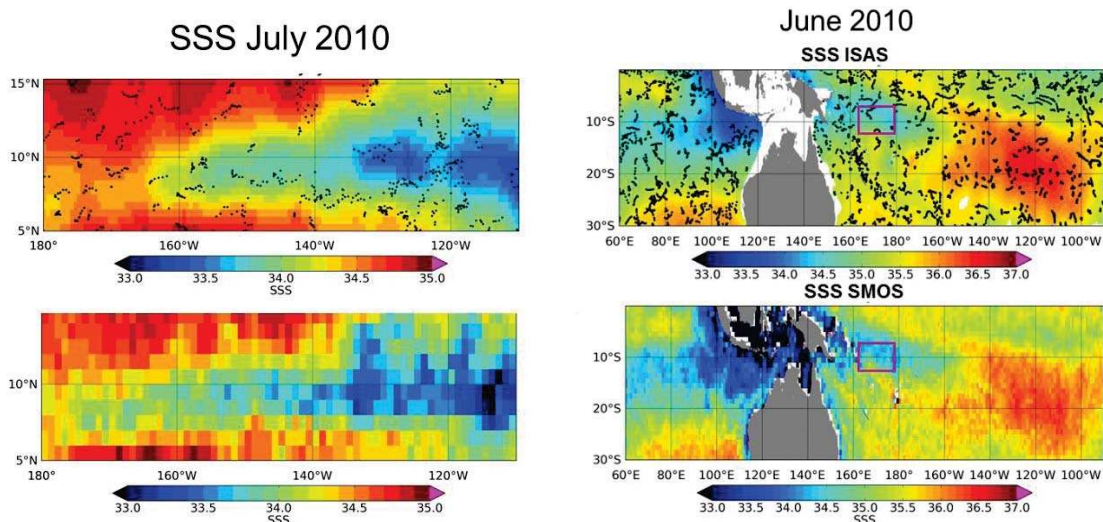
936 **Figure 21**: Rain Rate differences $\Delta RR = RR_{2011} - RR_{2010}$ derived from SSM/I F17 between
 937 2011 and 2010 for months of June (Top left); July (Bottom Left); October (Top right) and
 938 November (Bottom right).
 939

940 The differences in rain rate as derived from SSM/I F17 sensor between 2011 and 2010 for
 941 several selected months as shown in Figure 21 further demonstrate that part of the
 942 observed SSS interannual variability for July and November are associated with large
 943 precipitations anomalies during previous months, associated with displacements of the
 944 ITCZ and of the South Pacific Convergence Zone (SPCZ). In the Indian Ocean, SSS
 945 differences $\Delta SSS = SSS_{2011} - SSS_{2010}$ observed in November indicate saltier SSS in 2010 than
 946 in 2011 in the eastern equatorial Indian Ocean within the band [10°S-0°; 70°E-95°E]
 947 associated with a smaller rain rate ($RR_{2010} < RR_{2011}$) in the surrounding region during

948 preceding months, as evidenced by the rain rate difference on the October and November
 949 maps shown in Figure 21. Between $\sim 10^{\circ}\text{S}$ and 20°S , SSS are fresher in 2010 than in 2011;
 950 this is associated with higher precipitation in 2010 than in 2011 ($RR_{2011} < RR_{2010}$) in the
 951 eastern basin but not over the whole basin. Patterns of positive SSS anomalies in the
 952 eastern equatorial Indian Ocean, and negative anomalies in the eastern part of the region
 953 south of $\sim 10^{\circ}\text{S}$ are quite consistent with SSS anomalies already reported during negative
 954 IOD coupled with a strong La Niña event (see Figure 8 of Grunseich et al. 2011).

955

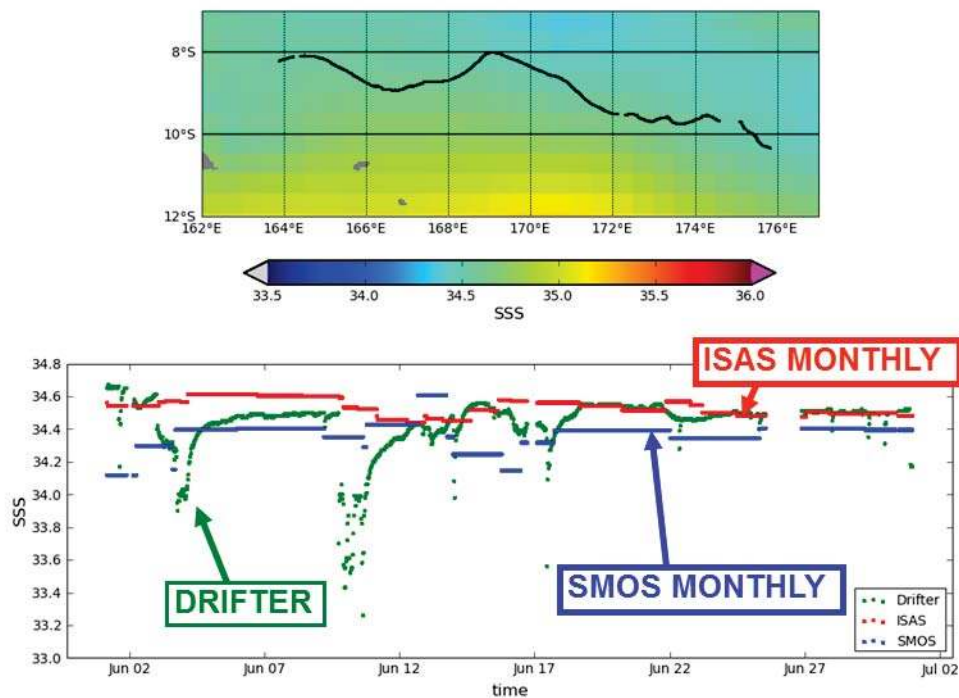
956 Although patterns of 2011-2010 SSS differences are similar on SMOS and ISAS monthly
 957 maps, the differences are often more contrasted in the SMOS data (e.g., Figure 20, left part
 958 and Figure 22).



959

960 **Figure 22:** Left: July 2010 SSS maps in the Northern Tropical Pacific Ocean from ISAS
 961 (top) and SMOS (bottom). Right: June 2010 SSS maps in south Pacific-Indian tropics from
 962 ISAS (top) and SMOS (bottom). In both top panels, the small black dots represent the
 963 locations of the *in situ* data samples used in the objective analysis. The purple square on
 964 the right figure indicates the region where the drifter discussed in Figure 23 evolved.
 965

966 This originates from fresher SSS seen in the SMOS SSS maps than in the ISAS SSS maps
 967 (Figure 22). In addition the spatial extent of the low SSS region appears wider in the
 968 SMOS map, as illustrated in Figure 22 left around 8°N . This is possibly due to the *in situ*
 969 measurements undersampling and/or smoothing by the OI applied to the ISAS. In addition,
 970 the SMOS freshening could be linked to the different depth of the measurements (SMOS at
 971 1cm, and *in situ* SSS measured at several meters depths) as described in sections 4.1 and
 972 4.2.



973

974 **Figure 23:**Top: trajectory of a Surface Velocity Program (SVP) float in the western
 975 Pacific region measuring conductivity and temperature at 45cm depth. Bottom: SSS along
 976 the drifter trajectory measured by the drifter (green), derived from SMOS monthly map
 977 (blue), from ISAS monthly map (red).

978

979 Finally, to illustrate the potential impact of the vertical stratification effect on the Δ SSS
 980 differences between satellite and *in situ*, we compare along the drifter trajectory the salinity
 981 measured at 45cm depth by a surface float (Reverdin et al. 2012) in the 2010 rainy western
 982 Pacific with monthly SSS maps (Figure 23). The drifter SSS data clearly indicates a large
 983 signature of rainy events, with typical freshening events larger than -1 and lasting for more
 984 than one day. The ISAS SSS is on the upper range of the drifter SSS while monthly SMOS
 985 SSS is systematically on the lower range in this rainy region. While more work is certainly
 986 needed to determine the physical sources for these observed differences, the vertical SSS
 987 stratification associated with rain events, as illustrated by this case, is a likely contributor to
 988 the different signatures in the inter-annual SSS variability as detected by the SMOS
 989 satellite SSS data and the Argo data.

990 These preliminary results confirm the capability of L-band radiometry in detecting large
 991 SSS signals and their low-frequency variability (here over a two-years period), in spite of
 992 much noisier satellite than *in situ* measurements. In general this results from much better
 993 satellite based spatio-temporal coverage and with a better spatial resolution, thus, offering
 994 complementary information to existing *in situ* measurements.

995

996 **5. Fresh Pools interactions with wind-driven processes**

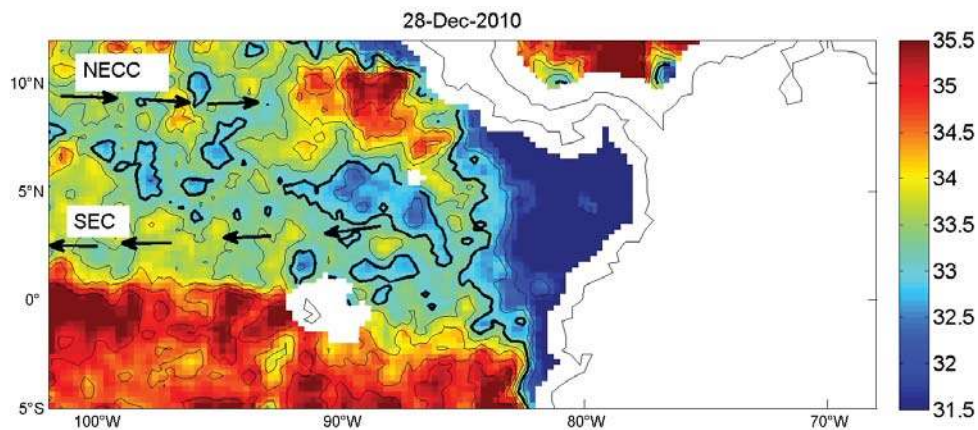
997 In this section, two specific SMOS observation cases study cases of wind-driven
998 phenomena are presented. The first example illustrates the erosion of the Far Eastern
999 Pacific Fresh Pool by the gap-wind driven Panama Upwelling processes whereas the
1000 second focuses on the salty wake left behind hurricanes after their passing over the
1001 Amazon-Orinoco river plumes.

1002

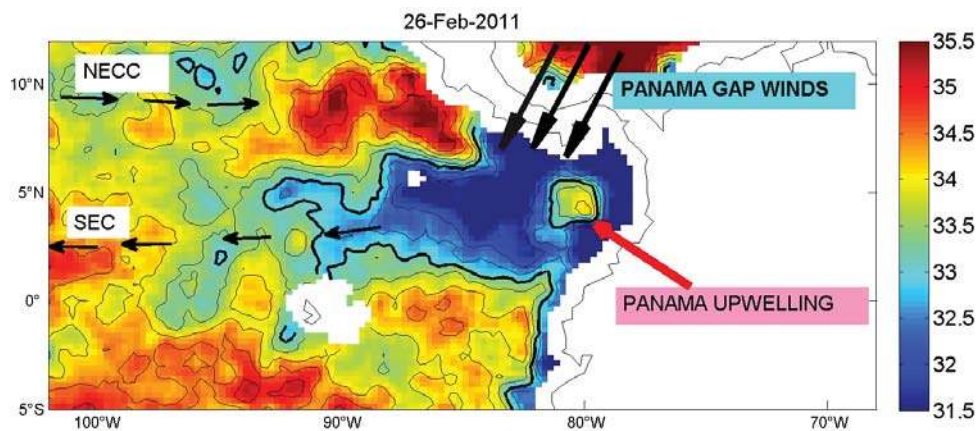
1003 **5.1 An example of Fresh Pool Erosion by wind-driven upwelling**

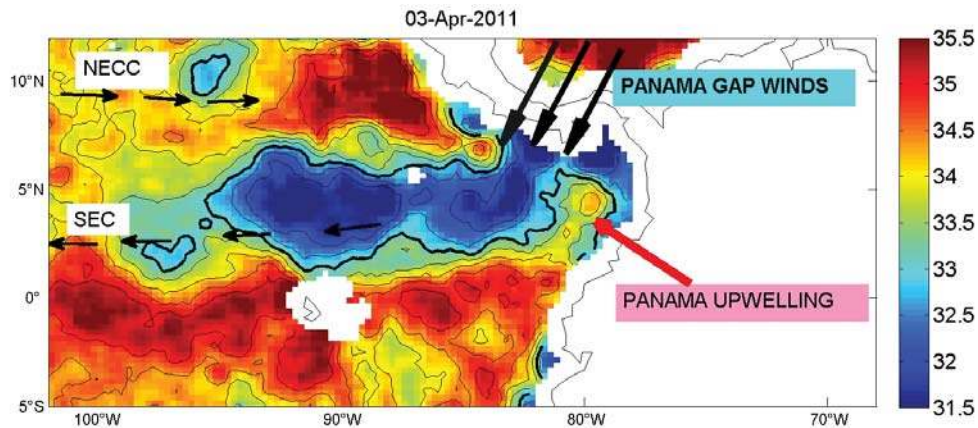
1004 The eastern tropical Pacific Ocean between about 120°W and South America is unique in
1005 many respects. Lying in an environment predominantly influenced by the South and North-
1006 Eastern trades and the doldrums, and seasonally affected by the winds from the Caribbean,
1007 this region is characterized by complicated and large seasonal variations in the wind field,
1008 current pattern, and temperature and salinity structure.

1009



1010





1011

1012 **Figure 24:** 10-days averaged SMOS SSS fields centered on the 28 Dec 2010 (Top), 16 Feb
 1013 2011 (middle) and 3 Apr 2011 (bottom). Small black arrows indicate the major surface
 1014 currents, namely the South Equatorial Current (SEC) and North Equatorial Counter
 1015 Current (NECC). Thick black contour is indicating the 32 isohaline.

1016

1017 The lowest sea surface salinity (SSS) of the tropical Pacific Ocean, the Easter Pacific Fresh
 1018 Pool (EPFP), is found between the warm pool characterized by a mean sea surface
 1019 temperature (SST) greater than 28°C centered around 15°N along the coast of Central
 1020 America and the cold and fresh equatorial region, with SSS values lower than 33 off the
 1021 Panama isthmus and lower than 34 extending as far as 130°W from the equator to 15°N
 1022 (Figure 24).

1023 The EPFP reflects both the conditions of excess precipitation over evaporation beneath the
 1024 ITCZ and input of fresh water from the Andes and Caribbean region (Benway and Mix,
 1025 2004). Analysis of a recent gridded *in situ* SSS product (Delcroix et al., 2011) points out
 1026 that interannual variations are relatively weak in the EPFP but that seasonal variations are
 1027 the strongest within the tropical Pacific. Large-scale analysis suggests that the SSS
 1028 seasonal balance is mostly driven by precipitation in the part of the EPFP covered by the
 1029 ITCZ, but more complex in the far east as advection and entrainment become important
 1030 processes (Bingham et al., 2010; Alory et al., 2012).

1031 By focusing on seasonal SSS variations along a well-sampled Voluntary Observing Ship
 1032 (VOS) line from Panama to Tahiti, Alory et al. (2012) recently showed that this fresh pool
 1033 dynamically responds to strong regional ocean-atmosphere-land interactions. First,
 1034 monsoon rains (and associated river runoff) give birth to the fresh pool in the Panama Bight
 1035 during summer and fall. Second, strong currents driven by topography-induced winds
 1036 extend the pool westward in winter while it eventually disappears by mixing with upwelled
 1037 saltier waters to the east. These dynamic features also generate steep SSS fronts at the
 1038 edges of the fresh pool (sometimes larger than ~4 psu/° of longitude at the eastern edges).

1039 These SSS fronts and the amplitude of their seasonal cycle are large enough to be detected
1040 by the new SMOS satellite mission. Compared to *in situ* data, SMOS satellite data provide
1041 a more homogeneous coverage with finer spatial resolution. Examples of SMOS SSS maps
1042 averaged over 10 days and centered at selected dates in December 2010, February and
1043 April 2011 are presented in Figure 24. Remarkably, all the major features observed with *in*
1044 *situ* VOS data as detailed in Alory et al. (2012) are well reproduced in the SMOS analysis,
1045 notably: the westward expansion of the fresh pool (SSS < 33) from 85°W in December to
1046 95°W in April, the steep SSS front east of the 32 isohaline and SSS minimum of 28 in the
1047 Panama Bight in December, and the strong SSS increase to around 35 in the Panama Bight
1048 in April. Moreover, SSS changes occurring between December and April are qualitatively
1049 consistent with the expected effects of winter climatological currents, including the
1050 Panama Bight upwelling.

1051 The freshwater pool disruption as observed by SMOS in the Panama bight (Figure 24,
1052 middle and bottom panels) are associated with the following processes: during the boreal
1053 winter, as the ITCZ moves southward, the north-easterly Panama gap wind creates a south-
1054 westward jet-like current in its path with a dipole of Ekman pumping/eddies on its flanks.
1055 As a result, upwelling in the Panama Bight brings cold and salty waters to the surface that
1056 erode the fresh pool on its eastern side while surface currents stretch the pool westward.

1057 Interestingly, SMOS data are also able to detect other meso-scale features in the
1058 region around the fresh pool such as the near-equatorial SSS front or the local SSS
1059 maximum in the Costa Rica dome.

1060 Therefore, SMOS SSS data will help in exploring qualitatively the seasonal
1061 dynamics of the fresh pools from their birth to their final erosion by wind-driven and
1062 turbulent processes (surface current stirring and wind-driven upwelling). Quantifying the
1063 relative contribution of the different mechanisms on SSS variations would require a
1064 model-based synergetic data analysis scheme to establish the mixed layer salt budget. Also,
1065 the regional occurrence of SSS fronts and barrier layers (de Boyer Montégut et al, 2007)
1066 suggests, by analogy with the western tropical Pacific, a link between surface and
1067 subsurface salinity which could give additional value to the satellite SSS data (Maes, 2008;
1068 Bosc et al., 2009). As barrier layers can play an active role on the tropical climate
1069 (e.g., Maes et al., 2002, 2005), studying their impacts in the region seems worthwhile. This
1070 could be done through regional modeling combined with analysis of subsurface/surface *in*
1071 *situ* and satellite data. Also, interannual variations of the fresh pool, even if quantitatively
1072 smaller than its seasonal variations, need further investigation as ENSO is a strong climate

1073 driver in the eastern Pacific. Now that 3 years of SMOS data are available, such type of
1074 analysis can be initiated.

1075

1076 **5.2 Fresh Pools interactions with Tropical Cyclones**

1077

1078 Because of the buoyant plume of fresh water that forms in the Atlantic due to discharge
1079 from the Amazon and Orinoco rivers, the North Western Tropical Atlantic (NWTA)
1080 region where the salt-driven upper ocean stratification may significantly impact ocean-
1081 atmosphere interactions under Tropical Cyclones. The spreading of the Amazon–Orinoco
1082 River plume exhibits a seasonal cycle coinciding with the Atlantic hurricane season (1
1083 June through 30 November) with river influenced minimum salinities observed farthest
1084 eastward and north westward during the height of the hurricane season (mid-August to
1085 mid-October). As shown by Ffield, (2007), for the 1960 to 2000 time period, 60% and
1086 68% of all category 4 and 5 hurricanes, respectively, passed directly over the likely plume
1087 region, revealing that the most destructive hurricanes may be influenced by plume–
1088 atmosphere interaction just prior to reaching the Caribbean. Historical *in situ* data reveal
1089 that average ocean surface temperatures first encountered by tropical cyclones moving
1090 westward between 12° and 20°N is only 26°C, but upon reaching the northern reaches of
1091 the Amazon–Orinoco River plume (e.g. see Figure 25), the average sea surface
1092 temperatures (SST) encountered by tropical cyclones are 2°C warmer. These warm ocean
1093 surface temperatures may play a role in hurricane maintenance and intensification since
1094 hurricanes can only form in extensive ocean areas with a surface temperature greater than
1095 25.5 deg C (Dare and McBride, 2011). In addition, as shown by Ffield (2007), the
1096 buoyant, and therefore stable, 10- to 60-m-thick layer of the plume can mask the presence
1097 and influence of other ocean processes and features just below the plume, in particular cool
1098 (during hurricane season) surface temperatures carried by NBC rings. After shedding from
1099 the NBC retroflection, the 300–500-km-diameter anticyclonic (clockwise) NBC rings pass
1100 northwestward through the Amazon–Orinoco River plume toward the Caribbean. The
1101 limited observations reveal that at times the cool upper-layer temperatures of the NBC
1102 rings are exposed to the atmosphere while at other times they are hidden just underneath
1103 warm plume water. Strong winds from the 300–1000-km-diameter cyclonic
1104 (counterclockwise) hurricanes might quickly erode a thin plume, exposing several degrees-
1105 cooler NBC ring water to the surface, and potentially contributing to limit further
1106 development of hurricanes. As shown by Ffields (2007), the warm temperatures associated

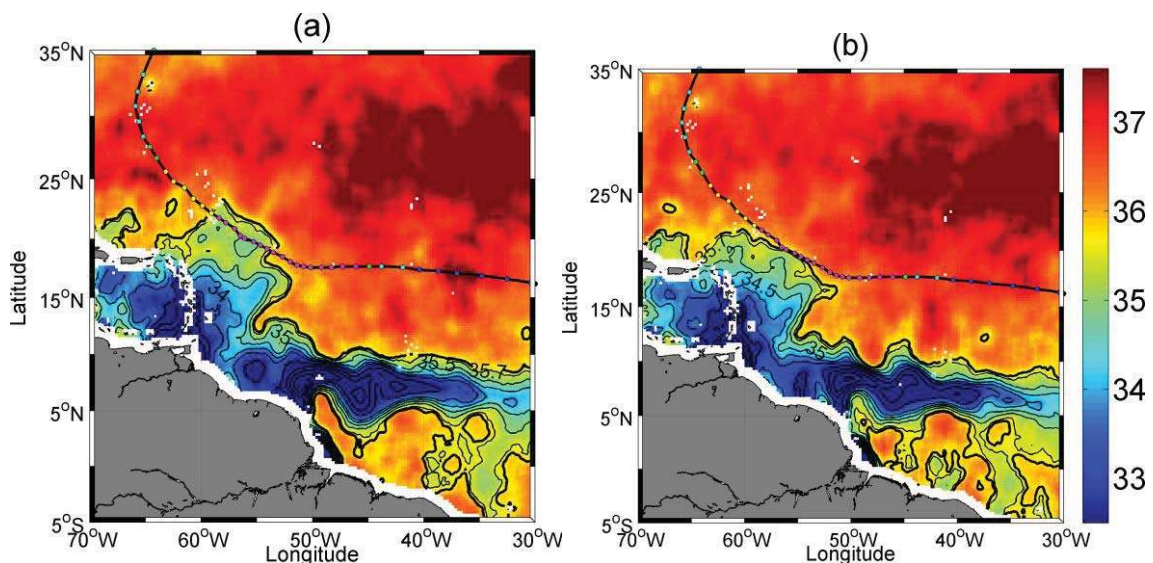
1107 with the low-salinity Amazon–Orinoco River plume and the relatively cool temperatures
1108 associated with NBC rings are in close proximity to the passing hurricanes. As such they
1109 are expected to actively influence on the hurricane maintenance and intensification
1110 although the interaction is challenging to accurately quantify.

1111 Vizy and Cook (2010) more recently studied the atmospheric response of the
1112 summertime large scale climate to the Amazon/Orinoco plume sea surface temperature
1113 anomaly forcing using a regional climate model. They performed simulations in the
1114 presence or absence of the Amazon/Orinoco plume SST anomalies. Results from their
1115 simulations indicate that the plume does significantly influence the frequency and intensity
1116 of summertime storm systems over the Atlantic, consistent with Ffield (2007). The
1117 presence of the plume increases the average number of Atlantic basin storms per summer
1118 by 60%. An increase in storm intensity also occurs, with a 61% increase of the number of
1119 storms that reach tropical storm and hurricane strength. Results from their simulations
1120 suggests that Atlantic storms also tend to curve northward further west in the Atlantic basin
1121 in presence of the plume SST anomaly. These results support the premise that the warm
1122 and low salinity combined Amazon-Orinoco River plume play an important role in
1123 modulating the air-sea interaction during hurricane passages in a manner similar to
1124 persistent fresh water barriers layers.

1125 For instance, when there is a fresh water barrier layer, such as in the North Western
1126 tropical Atlantic, mixing is restricted within shallower mixed layer and entrainment of cool
1127 thermocline water into the mixed layer is reduced (e.g., Anderson et al., 1996; Vialard and
1128 Delecluse, 1998a,b; Foltz and McPhaden, 2009). As discussed in Price (2009), if the net
1129 salinity anomaly (fresh water layer thickness times salinity anomaly in the initial state) is
1130 as large as about 20 m, then the fresh layer will potentially inhibit vertical mixing
1131 significantly. As the fresh water surface layer (halocline) of the Amazon and Orinoco river
1132 plumes is warmer than the water below (Ffield, 2007), salinity stratification acts to reduce
1133 the depth of vertical mixing and thus sea surface cooling. The reduced cooling amplitude
1134 in the wake of hurricanes passing over the Amazon and Orinoco river plume, associated
1135 with thick BL effects, might be an important mechanism in favor of hurricane
1136 intensification in that region. Similar impact of barrier-layers on TC-induced sea surface
1137 cooling have been recently evidenced for several case studies such as in the Tropical
1138 Atlantic (Balaguru et al. 2012), in the Bay of Bengal (Yu and McPhaden, 2011; Neethu et
1139 al., 2012) and in the tropical Northwest Pacific (Wang et al., 2011).

1140

1141 New insight into the interactions between such extreme atmospheric events and large-scale
 1142 fresh pools at the ocean surface has been gained from the satellite based SSS observations
 1143 as recently reported by Grodsky et al; (2012). They used data from the Aquarius/SAC-D
 1144 and SMOS satellites to help elucidate the ocean response to hurricane Katia, which crossed
 1145 the Amazon plume in early fall, 2011. As illustrated in their paper, the Katia passage left a
 1146 1.5 psu high haline wake covering $>10^5$ km² (in its impact on density, the equivalent of a
 1147 3.5°C cooling) due to mixing of the shallow BL.
 1148



1149 **Figure 25:** Two SMOS microwave satellite-derived SSS composite images of the Amazon
 1150 plume region revealing the SSS conditions (a) before and (b) after the passing of
 1151 Hurricane Igor, a category 4 hurricane that attained wind speeds of 136 knots in
 1152 September 2010 during its passage over the plume. Color-coded circles mark the
 1153 successive hurricane eye positions. Seven days of data centered on (a) 10 Sep 2010 and
 1154 (b) 22 Sep 2010 have been averaged to construct the SSS images, which are smoothed by a
 1155 1° x 1° block average.
 1156
 1157

1158 As illustrated in Figure 25, very similar observations were also detected from SMOS data
 1159 alone during the passage of the Category 4 hurricane Igor over the river plume in 2010.
 1160 The data evidence an erosion of the thin northern reach of the plume fresh surface layer by
 1161 Igor hurricane-induced mixing, covering an area of ~89000 km² located on the storm right-
 1162 hand side, where SSS increases by ~1 practical salinity unit whilst SST cools by 2-3°C.
 1163 On the left side of the storm, much smaller SSS and SST changes are detected after the
 1164 storm passage. The strong SSS increase in the hurricane wake within the plume is explained
 1165 by the erosion of the BL. This is supported by Argo profiles collected within the plume
 1166 (see Grodsky et al., 2012). Mixed layer salinity is lower by 2 to 4 psu than the water
 1167 beneath. The shallow haline stratification is destroyed by hurricane-forced entrainment

1168 which is stronger on the right side of hurricane eye (Price, 2009). It results in a strong SSS
1169 signal. Although the hurricane strengthened further along the trajectory, the SSS change is
1170 much weaker there corresponding to weak vertical salinity stratification outside the plume.
1171 As further discussed in Grodsky et al., 2012, the fresh (more buoyant) BL limits the
1172 turbulent mixing and then the SST cooling in the plume, and thus preserved higher SST
1173 and fresh water evaporation than outside. Combined with SST, the new satellite SSS data
1174 thus provide a new and better tool to monitor the plume extent and quantify the upper
1175 ocean responses to tropical cyclones with important implications for hurricane forecasting.

1176

1177 **6. Conclusions& Perspectives**

1178

1179 The ocean is the primary return conduit for water transported by the atmosphere. It is the
1180 dominant element of the global water cycle, and clearly one of the most important
1181 components of the climate system, with more than 1100 times the heat capacity of the
1182 atmosphere. Two new satellite sensors, the ESA Soil Moisture and Ocean Salinity Mission
1183 (SMOS) and the NASA Aquarius SAC-D missions are now providing the first space borne
1184 measurements of the sea surface salinity (SSS). Synergetic analyses of the new surface
1185 salinity data sets together with sea surface temperature, dynamic height and surface
1186 geostrophic currents from altimetry, near surface wind, ocean color, in situ observations,
1187 and rainfall estimates will certainly help clarifying the fresh water budget in key oceanic
1188 tropical areas.

1189 In this paper, we selected illustrative examples to review how the first SSS products
1190 derived from the SMOS sensor can readily help to better characterize some of the key
1191 processes of the marine branch of the global hydrological cycle. First, we illustrated the
1192 new monitoring capabilities for some of the world largest oceanic fresh water pools
1193 generated by the discharge of very large tropical rivers. In particular, we show how SMOS
1194 SSS traces the fresh water signals from the Amazon-Orinoco and Congo river
1195 plumes. River runoff is an important variable in oceanography as their fresh water affects
1196 SSS and the buoyancy of the surface layer, and they represent a source of materials exotic
1197 to the ocean and highly important to biological activity. Obviously, they are key
1198 hydrologic components of the fresh water exchanges between the atmosphere, land and
1199 ocean. Despite this importance, tracing river fresh water transport over large distances has
1200 not been straightforward previously principally because of a lack of SSS data. Tracing
1201 those very large rivers over great distances now become an important endeavor, as

1202 sufficient data are available from the SMOS and Aquarius sensors that can be further
1203 combined with satellite derived surface geostrophic current data.

1204 Second, we evidenced key oceanic precipitation signatures in the SMOS SSS signal.
1205 Satellite radiometry at L-band provides for the first time a global measure of the salinity at
1206 the ocean-atmosphere interface (within the upper centimeters). Rain events induce
1207 freshening of the ocean surface and are responsible for a high temporal variability in the
1208 SSS, consistently detected by both *in situ* and spaceborne sensors. Because of the vertical
1209 haline gradient generated by the rain-induced freshening in the upper ocean, fresher
1210 surface waters are however systematically found from space in rainy area compared with
1211 the 1-10 m depth *in situ* data. These differences challenge calibration/validation activities
1212 of the satellite SSS in high precipitation regions. Nevertheless, satellite SSS data certainly
1213 provide new information about ocean-atmosphere interfacial fresh water fluxes in these
1214 conditions. This was evidenced by comparing spatial patterns and amplitudes of the large
1215 scale SSS anomalies estimated from the SMOS data and the net Evaporation minus
1216 Precipitation fluxes in the Tropical Atlantic. Under the InterTropical Convergence Zone
1217 and sufficiently far away from the river runoff signals, residual SSS anomalies were shown
1218 to be highly correlated to the *E-P* anomalies. In particular, SSS anomalies become
1219 increasingly negative as the Precipitation anomalies progressively exceed the Evaporation
1220 anomalies. This demonstrate the importance of monitoring SSS from space in rainy
1221 regions, suggesting that the interfacial SSS values might be a good large-scale oceanic rain
1222 gauge of the global hydrological water cycle.

1223 The interfacial character of the spaceborne measurements also offer new information of
1224 interest for ocean circulation models in the perspective of better constraining oceanic
1225 precipitation forcing terms.

1226 Finally, the SSS observations from SMOS satellite were used to reveal new aspect
1227 of the main tropical fresh pool evolution and interaction with wind-driven atmospheric
1228 processes. SMOS imagery thus captures how the large Eastern Pacific Fresh Pool is
1229 systematically eroded at the end of the boreal summer on its eastern side by the wind-
1230 driven Panama Upwelling which brings cold and salty waters to the surface. Prior to
1231 SMOS data availability, the few existing studies of the eastern Pacific describing seasonal
1232 variations of SSS did not investigate their cause beyond rainfall (e.g., Fiedler and Talley,
1233 2006). Thanks to the new SMOS data, SSS variability associated with wind-driven
1234 processes in that region, such as the Panama upwelling signal recently evidenced by Alory
1235 et al. (2012), can now be characterized more deeply.

1236 Because of the buoyant character of the fresh water that forms at the ocean surface
1237 due to large river discharges or intense local precipitation, the upper ocean stratification in
1238 several key tropical oceans regions (e.g., North Western Tropical Atlantic, Eastern and
1239 Western Pacific Fresh Pools, Bay of Bengal) is mostly controlled by salinity. In such
1240 freshwater pool regions, a uniform density mixed layer is found to form the so-called
1241 Barrier Layers at shallower depth than the uniform temperature layer. Because of stable
1242 halocline, the BL are acting to inhibit surface cooling and vertical mixing under the action
1243 of surface wind stresses. Therefore, there can be some feedback mechanisms between
1244 atmospheric, or terrestrial, fresh water fluxes to the ocean and intense atmospheric
1245 processes. About 68% of hurricanes that finally reached category 4 and 5 have thus crossed
1246 the Amazon/Orinoco plume [Ffield, 2007] where the presence of Barrier Layers can
1247 enhance their growth rate by 50% [Balaguru et al., 2012]. Under an intense hurricane, the
1248 halocline, which is above the thermocline, is first mixed. This produces a SSS wake that is
1249 by a few psu saltier than initial SSS in the plume. By analysing SMOS SSS data before
1250 and after the passage of several intense hurricanes over the Amazon river plume in 2010
1251 and 2011, SSS changes >1 psu over areas exceeding 10^5 km² were detected. These abrupt
1252 changes have implications for SSS climate, since SSS is more long-lived and not damped
1253 like SST. In addition, destruction of the BL is apparently associated with a decreased SST
1254 cooling in the plume that, in turn, preserves higher SST and evaporation than outside the
1255 BL. This difference in SST cooling is explained by additional work required to mix the
1256 BL. Thus BL leads to a reduction in hurricane-induced surface cooling that favors
1257 hurricane intensification, as the resulting elevated SST and high evaporation enhance the
1258 hurricane's maximum potential intensity. The geographic location and seasonality of the
1259 Amazon/Orinoco plume make hurricane overpasses a frequent occurrence. Indeed, the
1260 expansion of the plume in August-September coincides with the peak of the production of
1261 Cape Verde hurricanes, which includes many of the most intense (Category 4–5)
1262 hurricanes. Thus the results presented here strongly suggest that the role of the salinity
1263 stratification in mixed layer dynamics should be taken into account when forecasting
1264 tropical cyclone growth over freshwater pools that are generating thick BL (Amazon
1265 plume, Bay of Bengal, Eastern and Western Pacific Fresh Pools). The availability of
1266 satellite SSS from Aquarius and SMOS along with in situ Argo measurements is critical to
1267 making such model improvements practical.

1268

1269

1270 **Acknowledgements**

1271 Work presented in this paper was partly done under ESA support in the context of the
1272 development of the SMOS Level 2/Expert Support Laboratory, ESA Support to Science
1273 Element SMOS+SOS and SMOS+STORM projects. CNES also partly funded these
1274 activities in the frame of the Centre Aval de Traitement des Données SMOS (CATDS)
1275 and of the SMOS/ESA GLOSCAL Cal/Val projects. We are indebted to Micha Rijkenberg
1276 (Koninklijk Nederlands Instituut voor Onderzoek der Zee · Department of Biological
1277 Oceanography (BIO)) for giving us access to the Geotraces Leg 2 CTD data, to F. Gaillard
1278 (LPO/IFREMER) for providing ISAS maps version 6 (see [http://wwz.ifremer.fr/lpo/SO-](http://wwz.ifremer.fr/lpo/SO-Argo/Products/Global-Ocean-T-S)
1279 [Argo/Products/Global-Ocean-T-S](http://wwz.ifremer.fr/lpo/SO-Argo/Products/Global-Ocean-T-S)). Gilles Reverdin (LOCEAN/CNRS) is responsible for
1280 french salinity drifter deployment program, he supervised the quality control of these
1281 drifter data set and is warmly acknowledged. These data are available on [www.locean-](http://www.locean-ipsl.upmc.fr/smos/drifters)
1282 [ipsl.upmc.fr/smos/drifters](http://www.locean-ipsl.upmc.fr/smos/drifters). We thank Nicolas Martin for data processing. We are also
1283 indebted to Jérôme Vialard, Matthieu Lengaigne and Emmanuel Vincent for their very
1284 helpful comments about SSS variability in the tropical Indian Ocean and about Tropical
1285 Cyclones interactions with the Amazon plume, Thierry Delcroix about SSS variability in
1286 the tropical Pacific Ocean. SSM/I data have been processed by Remote Sensing System
1287 (www.ssmi.com). The global ocean heat flux and evaporation products were provided by
1288 the WHOI OAFlux project (<http://oaflux.whoi.edu>) funded by the NOAA Climate
1289 Observations and Monitoring (COM) program.

1290

1291 **References**

- 1292 Alory G, Maes C, Delcroix T, Reul N, Illig S (2012), Seasonal dynamics of sea surface
1293 salinity off Panama: the far eastern Pacific fresh pool, *J. Geophys. Res.* 117:
1294 C04028
- 1295 Anderson SP, Weller RA, Lukas R (1996) Surface Buoyancy Forcing and the Mixed Layer
1296 of the Western Pacific Warm Pool: Observations and 1D Model Results. *J.*
1297 *Climate*, **9**, 3056–3085
- 1298 Baklouti M, Devenon JL, Bourret A, Froidefond JM, Ternon JF, Fuda JL (2007) New
1299 insights in the French Guiana continental shelf circulation and its relation to the
1300 North Brazil Current retroflexion, *J. Geophys. Res.* 112: C02023
- 1301 Balaguru KP, Saravanan SR, Leung LR, Xu Z, Li M, Hsieh JS, (2012) Ocean barrier
1302 layers' effect on tropical cyclone intensification, *PNAS*,
1303 doi:10.1073/pnas.1201364109
- 1304 Banks CJ, Gommenginger CP, Srokosz MA., Snaith HM (2012) Validating SMOS ocean
1305 surface salinity in the atlantic with Argo and operational ocean model data, *IEEE*
1306 *Transactions on Geoscience and Remote Sensing* 50: 1688–1702

- 1307 Benway HM, Mix AC (2004) Oxygen isotopes, upper-ocean salinity, and precipitation
1308 sources in the eastern tropical Pacific, *Earth Planet. Sci. Lett.*, 224: 493–507
- 1309 Binet D, Marchal E (1993) The Large Marine Ecosystem of Shelf Areas in the Gulf of
1310 Guinea: Long-Term Variability Induced by Climatic Changes. In Kenneth Sherman,
1311 et al. (eds.), *Large Marine Ecosystems: Stress, Mitigation, and Sustainability*
1312 (Washington, D.C.: American Association for the Advancement of Science, 1993) :
1313 104-118.
- 1314 Bingham FM, Foltz GR, McPhaden MJ (2010), Seasonal cycles of surface layer salinity in
1315 the Pacific Ocean, *Ocean Sci.*, 6: 775–787
- 1316 Blough NV, Del Vecchio R (2002), Chromophoric DOM in the coastal environment, in
1317 *Biogeochemistry of Marine Dissolved Organic Matter*, edited by D. A. Hansell, and
1318 C. A. Carlson, pp. 509–546, Academic, San Diego, Calif
- 1319 Bonjean F, Lagerloef GSE (2002): Diagnostic Model and Analysis of the Surface Currents
1320 in the Tropical Pacific Ocean. *J. Phys. Oceanogr.* (32): 2938–2954
- 1321 Bornhold BD (1973) Late Quaternary sedimentation in the eastern Angola Basin.
1322 Massachusetts Institute of Technology: 1-213 (thesis).
- 1323 Bosc C, Delcroix T, Maes C (2009) Barrier layer variability in the western Pacific warm
1324 pool from 2000 to 2007, *J. Geophys. Res.*, 114, C06023
- 1325 Boutin J, Martin N, Yin X, Reul N, Spurgeon P (2012a) First Assessment of SMOS Data
1326 Over Open Ocean: Part II-Sea Surface Salinity. *IEEE Transactions on Geoscience*
1327 *and Remote Sensing* 50 (5) Part 1: 1662 - 1675
- 1328 Boutin J, Martin N, Reverdin G, Yin X, Gaillard F (2012b), Sea surface freshening
1329 inferred from SMOS and Argo salinity: Impact of rain, *Ocean Sci. Discuss.*, 9,
1330 3331-3357
- 1331 Boyer TP, Levitus S (2002) Harmonic analysis of climatological sea surface salinity, *J.*
1332 *Geophys. Res.*, 107(C12): 8006
- 1333 Braga ES, Andrie C, Bourles B, Vangriesheim A, Baurand F, Chuchla R (2004) Congo
1334 River signature and deep circulation in the eastern Guinea Basin. *Deep Sea*
1335 *Research Part I: Oceanographic Research Papers* 51 (8): 1057-1073.
- 1336 Carval T, Keeley B, Takatsuki Y, Yoshida T, Loch S, Schmid, C, Goldsmith R, Wong A,
1337 McCreddie R, Thresher A, Tran A (2012) *Argo User's Manual v2.4*, 85, IFREMER
1338 referencecor-do/dti-mut/02-084
- 1339 Cherubin LM, Richardson PL (2007) Caribbean Current Variability And The Influence Of
1340 The Amazon And Orinoco Freshwater Plumes, *Deep-Sea Research Part I-*
1341 *Oceanographic Research Papers*, 54(9): 1451-1473
- 1342 Conmy RN, Coble PG, Cannizzaro JP, Heil CA (2009) Influence of extreme storm events
1343 on West Florida Shelf CDOM distributions, *J. Geophys. Res.*, 114, G00F04
- 1344 Cravatte S, Delcroix T, Zhang D, McPhaden MJ, Leloup J (2009). Observed freshening
1345 and warming of the western Pacific warm pool. *Clim. Dyn.* 33, 565–589

- 1346 Dare RA., McBride JL(2011) The Threshold Sea Surface Temperature Condition for
1347 Tropical Cyclogenesis. *J. Climate*, 24: 4570–4576.
- 1348 Del Vecchio R, Subramaniam A (2004) Influence of the Amazon River on the surface
1349 optical properties of the Western Tropical North Atlantic Ocean, *J. Geophys. Res.*,
1350 109, C11001
- 1351 De Boyer Montégut C, Mignot J, Lazar A, Cravatte S (2007), Control of salinity on the
1352 mixed layer depth in the world ocean: 1. General description, *J. Geophys. Res.*,
1353 112, C06011
- 1354 Delcroix T, Alory G, Cravatte S, Corrège T, McPhaden MJ (2011) A gridded sea surface
1355 salinity data set for the tropical Pacific with sample applications (1950–2008), *Deep
1356 Sea Res., Part I* 58(1): 38–48
- 1357 DeMaster D J, Smith W, Nelson DM, Aller JY (1996), Biogeochemical processes in
1358 Amazon shelf waters: Chemical distributions and uptake rates of silicon, carbon
1359 and nitrogen, *Cont. Shelf Res.*, 16: 617–643
- 1360 Dessier A, Donguy J (1994) The Sea-Surface Salinity In The Tropical Atlantic Between
1361 10-Degrees-S And 30-Degrees-N - Seasonal And Interannual Variations (1977-
1362 1989), *Deep-Sea Research Part I-Oceanographic Research Papers*, 41(1): 81-100
- 1363 Dickson RR, Yashayaev I, Meincke J, Turrell W, Dye S, Holfort J (2002) Rapid freshening
1364 of the deep North Atlantic Ocean over the past four decades. *Nature* 416: 832-837
- 1365 Donguy JR, Hénin C (1980) Surface conditions in the eastern equatorial Pacific related to
1366 the intertropical convergence zone of the winds, *Deep Sea Res., Part A*, 27: 693–
1367 714
- 1368 D'Sa EJ, Hu C, Muller-Karger FE, Carder KL (2002) Estimation of colored dissolved
1369 organic matter and salinity fields in case 2 waters using SeaWiFS: Examples
1370 from Florida Bay and Florida Shelf, *J. Earth Syst. Sci.*, 111: 197–207
- 1371 Durack PJ, Wijffels SE, Matear RJ (2012) Ocean salinities reveal strong global water cycle
1372 intensification during 1950 to 2000, *Science* 336: 455–458
- 1373 Eisma D, Van Bennekom A.J. (1978) The Zaire river and estuary and the Zaire outflow in
1374 the Atlantic ocean. *Netherlands Journal of Sea Research* 12 (3/4), 255–272.
- 1375 Ferrari GM, Dowell MD (1998) CDOM absorption characteristics with relation to
1376 fluorescence and salinity in coastal areas of the southern Baltic Sea, *Estuarine
1377 Coastal Shelf Sci.*, 47, 91–105
- 1378 Ffield A (2005) North Brazil Current rings viewed by TRMM Microwave Imager SST and
1379 the influence of the Amazon Plume. *Deep-Sea Res. I*, 52: 137–160
- 1380 Ffield A, (2007) Amazon and Orinoco River plumes and NBC Rings: bystanders or
1381 participants in hurricane events? *J. Clim.* 20: 316-333
- 1382 Fiedler PC, Talley LD (2006), Hydrography of the eastern tropical Pacific: A review, *Prog.
1383 Oceanogr.*, 69(2–4): 143–180

- 1384 Flagg CN, Gordon RL, McDowell S (1986) Hydrographic and current observations on the
1385 continental slope and shelf of the western equatorial atlantic, *Journal of Physical*
1386 *Oceanography* 16(8): 1412-1429
- 1387 Foltz GR, McPhaden JM (2009) Impact of barrier layer thickness on SST in the central
1388 tropical North Atlantic. *J. Climate* 22: 285-299
- 1389 Font J, Camps A, Borges A, Martín-Neira M, Boutin J, Reul N, Kerr YH, Hahne A,
1390 Mecklenburg S (2010) SMOS: The Challenging Sea Surface Salinity Measurement
1391 from Space, *Proceedings of the IEEE* 98(5):649-665
- 1392 Font J, Boutin J, Reul N, Spurgeon P, Ballabrera-Poy J, Chuprin A, Gabarró C, Gourrion
1393 J, Guimbarde S, Hénocq C, Lavender S, Martin N, Martínez J, McCulloch M,
1394 Meirold-Mautner I, Mugerin C, Petitcolin F, Portabella M, Sabia R, Talone M,
1395 Tenerelli J, Turiel A, Vergely JL, Waldteufel P, Yin X, Zine X, Delwart S
1396 (2013) SMOS first data analysis for sea surface salinity determination,
1397 *International Journal of Remote Sensing*, DOI:10.1080/01431161.2012.716541
- 1398 Froelich PN, Atwood DK, Giese GS (1978) Influence of amazon river discharge on
1399 surface salinity and dissolved silicate concentration in the caribbean sea, *Deep Sea*
1400 *Research*,25(8):735-744
- 1401 Gaillard F, Autret E, Thierry V, Galaup P, Coatanoan C, Loubrieu T (2009) Quality
1402 control of large Argo datasets, *J. Atmos. Ocean. Tech.*, 26, 337–351
- 1403 Garzoli SL, Field A, Johns WE, Yao Q (2004) North Brazil Current retroflection and
1404 transports, *J. Geophys. Res.*, 109, C01013
- 1405 Goni GJ, Johns W (2001) A Census of North Brazil Current Rings Observed from T/P
1406 Altimetry: 1992-1998, *Geophys. Res. Lett.*, 1-4
- 1407 Gordon A, Guilvi CF (2008) Sea surface salinity trends over 50 years within the
1408 subtropical North Atlantic. *Oceanography* 20 (1): 20-29
- 1409 Gouriou Y, Delcroix T (2002) Seasonal and ENSO variations of sea surface salinity and
1410 temperature in the South Pacific Convergence Zone during 1976–2000. *Journal of*
1411 *Geophysical Research* 107: 3185
- 1412 Grodsky SA, Reul N, Lagerloef G, Reverdin G, Carton JA, Chapron B, Quilfen Y,
1413 Kudryavtsev VN, Kao HY (2012) Haline hurricane wake in the Amazon/Orinoco
1414 plume: AQUARIUS/SACD and SMOS observations, *Geophys. Res. Lett.*, 39,
1415 L20603
- 1416 Grunseich G, Subrahmanyam B, Murty VSN, Giese BS (2011) Sea surface salinity
1417 variability during the Indian Ocean Dipole and ENSO events in the tropical Indian
1418 Ocean, *J. Geophys. Res.*, 116: C11013
- 1419 Hellerman S, Rosenstein M (1983), Normal monthly wind stress over the world ocean with
1420 error-estimates, *Journal Of Physical Oceanography*, 13(7): 1093-1104
- 1421 Hellweger F, Gordon A (2002), Tracing Amazon River water into the Caribbean Sea,
1422 *Journal of Marine Research*, 60 : 537-549

- 1423 Hisard P, (1980) Observation de réponses de type "El Niño" dans l'Atlantique tropical
1424 oriental, Golfe de Guinée. *Oceanol.Acta* 3: 69-78
- 1425 Hu C, Montgomery ET, Schmitt RW, Muller-Karger FE (2004) The dispersal of the
1426 Amazon and Orinoco River water in the tropical Atlantic and Caribbean Sea:
1427 Observation from space and S-PALACE floats, *Deep Sea Res. Part II*, 51: 1151–
1428 1171.
- 1429 Johns, WE, Lee TN, Schott FA, Zantopp RJ, Evans RH (1990) The north Brazil current
1430 retroflection: Seasonal structure and eddy variability, *J. Geophys. Res.* 95: 22103-
1431 22120
- 1432 Katsaros KB, Buettner K JK (1969) Influence of Rainfall on Temperature and Salinity at
1433 the Ocean Surface, *J. Appl. Meteorol.* 8: 15–18.
- 1434 Kerr Y, Waldteufel P, Wigneron JP, Delwart S, Cabot F, Boutin J, Escorihuela MJ, Font J,
1435 Reul N, Gruhier C (2010) The SMOS Mission: New Tool for Monitoring Key
1436 Elements of the Global Water Cycle. *Proceedings of the IEEE* 98(5): 666-687
- 1437 Klein LA, Swift CT (1977) Improved model for dielectric constant of seawater at
1438 microwave frequencies. *IEEE Transactions on Antennas and Propagation* 25: 104-
1439 111.
- 1440 Koleshnikov AG (1973) Equalant I and Equalant II, *Physical oceanography*. UNESCO,
1441 Paris 1: 1-289
- 1442 Lagerloef GSE, Mitchum G, Lukas R, Niiler P (1999) Tropical Pacific near surface
1443 currents estimated from altimeter, wind and drifter data. *J. Geophys. Res.*,
1444 104: 23,313-23,326
- 1445 Lagerloef GSE, Colomb FR, Le Vine D, Wentz F, Yueh S, Ruf C, Lilly J, Gunn J, Chao Y,
1446 deCharon A, Feldman G, Swift C (2008) The Aquarius/SAC-D Mission: Designed
1447 to meet the salinity remote-sensing challenge. *Oceanography* 21(1):68–81
- 1448 Lagerloef GSE, Boutin J, Chao Y, Delcroix T, Font J, Niiler P, Reul N, Riser S, Schmitt R,
1449 Stammer D, Wentz F (2010) Resolving the Global Surface Salinity Field and
1450 Variations by Blending Satellite and In Situ Observations, *Oceanobs'09: Sustained
1451 Ocean Observations and Information for Society*, Venice, Italy, 21–25 September
1452 2009, ESA Publication WPP-306
- 1453 Lagerloef GSE (2012) Satellite mission monitors ocean surface salinity, *Eos Trans. AGU*
1454 93(25), 233, doi:10.1029/2012EO250001.
- 1455 Lefèvre N (2009) Low CO₂ concentrations in the gulf of guinea during the upwelling
1456 season in 2006, *Marine Chemistry*, 113(1-2), 93
- 1457 Lentz SJ (1995) Seasonal-Variations In The Horizontal Structure Of The Amazon Plume
1458 Inferred From Historical Hydrographic Data, *J. Geophys. Res.*, 100(C2): 2391-2400
- 1459 Lentz SJ, Limeburner R (1995) The Amazon River Plume during AMASSEDS: Spatial
1460 characteristics and salinity variability, *J. Geophys. Res.*, 100: 2355–2375

- 1461 Maes C (2008) On the ocean salinity stratification observed at the eastern edge of the
1462 equatorial Pacific warm pool, *J. Geophys. Res.*, 113, C03027
- 1463 Maes C, Picaut J, Belamari S (2002) Salinity barrier layer and onset of El Niño in a Pacific
1464 coupled model, *Geophys. Res. Lett.*, 29(24), 2206
- 1465 Maes C, Picaut J, Belamari S (2005), Importance of salinity barrier layer for the buildup of
1466 El Niño, *J. Clim.*, 18, 104–118
- 1467 Meade RH, Nordin CF, Hernandez DP, Mejia A, Godoy JMP (1983) Sediment and water
1468 discharge in Rio Orinoco, Venezuela and Colombia. In: *Proceedings of the Second*
1469 *International Symposium on River Sedimentation. Water resources and Electric*
1470 *Power Press, Beijing, China, pp. 1134–1144.*
- 1471 Mecklenburg S, Drusch M, Kerr YH, Font J, Martin-Neira M, Delwart S, Buenadicha G,
1472 Reul N, Daganzo-Eusebio E, Oliva R, Crapolicchio R (2012) ESA's Soil Moisture
1473 and Ocean Salinity Mission: Mission Performance and Operations, *IEEE*
1474 *Transactions on Geoscience and Remote Sensing* 50 (5) Part 1: 1354 - 1366
- 1475 Merle J, (1980) Variabilité thermique annuelle et interannuelle de l'océan Atlantique
1476 équatorial est. L'hypothèse d'un " El Niño " Atlantique. *Oceanol. Acta* 3, 209-220
- 1477 Meulenbergh J (1968) Diffusion des eaux du fleuve Congo dans les eaux de l'Atlantique
1478 Sud. *Acad. roy. SC. Outre-Mer, SC. Te&., N.S. SVI (6) Bruxelles*, 148 p.
- 1479 Meybeck M, Ragu A (1997) River discharges to the oceans: An assessment of suspended
1480 solids, major ions, and nutrients, *IAHS Publ.*, 243: 1–245
- 1481 Michel S, Chapron B, Tournadre J, Reul N (2007) Sea surface salinity variability from a
1482 simplified mixed layer model of the global ocean, *Ocean Sci. Discuss.*, 4: 41–106
- 1483 Mignot J, de Boyer Montégut C, Lazar A, Cravatte S (2007) Control of salinity on the
1484 mixed layer depth in the world ocean: 2. Tropical areas. *J. Geophys. Res.*, 112,
1485 C10010
- 1486 Miller R, Zepp RG (1995) Photochemical production of dissolved inorganic carbon from
1487 terrestrial organic matter: Significance to the oceanic organic carbon cycle,
1488 *Geophys. Res. Lett.*, 22, 417–420
- 1489 Milliman JD, Meade RH (1983) World-wide delivery of river sediment to the oceans, *The*
1490 *Journal of Geology*, 91(1): 1-21
- 1491 Moller GSF, de M. Novo EML, Kampel M (2010), Space-time variability of the Amazon
1492 River plume based on satellite ocean color, *Continental Shelf Research* 30(3–4):,
1493 342-352
- 1494 Moran M A, Sheldon WM, Sheldon JE (1999), Biodegradation of riverine dissolved
1495 organic carbon in five estuaries of the southeastern United States, *Estuaries*, 22: 55–
1496 64
- 1497 Morrow R, Valladeau G, Sallee J-B (2008) Observed subsurface signature of Southern
1498 Ocean sea level rise. *Prog. Oceanogr.* 77(4): 351–366

- 1499 Muller-Karger FE, McClain CR, Richardson PL (1988) The dispersal of the Amazon's
1500 water, *Nature*, 333 : 56–59
- 1501 Muller-Karger FE, McClain CR, Fisher TR, Esaias WE, Varela R(1989) Pigment
1502 distribution in the Caribbean Sea: Observations from space, *Prog. Oceanogr.*, 23:
1503 23–64
- 1504 Muller-Karger FE, Richardson PL, McGillicuddy D (1995), On the offshore dispersal of
1505 the Amazon's Plume in the North Atlantic, *Deep Sea Res. Part I*, 42: 2127–2137
- 1506 Neetu S, Lengaigne M, Vincent EM, Vialard J, Madec G, Samson G, Ramesh Kumar MR,
1507 Durand F (2012) Influence of upper-ocean stratification on tropical cyclones-
1508 induced surface cooling in the Bay of Bengal. *Journal of Geophysical Research*,
1509 117, C12020
- 1510 Neumann G (1969) Seasonal salinity variations in the upper strata of the western tropical
1511 Atlantic ocean-I. Sea surface salinities, *Deep-Sea Res.* 16: 165-177
- 1512 Nittrouer CA, Demaster DJ (1986), Sedimentary processes on the Amazon continental
1513 shelf: past, present and future research, *Continental Shelf Research*, 6: 5-30
- 1514 Obernosterer I, Herndl GJ (2000) Differences in the optical and biological reactivity of the
1515 humic and non-humic DOC component in two contrasting coastal marine
1516 environments, *Limnol. Oceanogr.*, 45: 1120–1129
- 1517 Ostapoff F, Tarbeyev Y, Worthem S (1973) Heat Flux and Precipitation Estimates from
1518 Oceanographic Observations, *Science* 180: 960–962.
- 1519 Palacios SL, Peterson TD, Kudela RM (2009), Development of synthetic salinity from
1520 remote sensing for the Columbia River Plume, *J. Geophys. Res.*, 114: C00B05
- 1521 Perry GD, Duffy PB, Miller NL (1996) An extended data set of river discharges for
1522 validation of general circulation models, *J. Geophys. Res.* 101: 21339-21349
- 1523 Piterbarg LI, Ostrovskii AG(1997) Advection and Diffusion in Random Media:
1524 Implications for Sea Surface Temperature Anomalies. Kluwer Academic, 330 pp.
- 1525 Piton B, Wacongne S (1985). Unusual amounts of very saline subsurface water in the
1526 eastern Gulf of Guinea in May 1984. *Tropical Ocean-Atmosphere Newsletter* 325-8
- 1527 Price JF (2009) Metrics of hurricane-ocean interaction: Vertically-integrated or vertically-
1528 averaged ocean temperature? *Ocean Science* 5:351–368.
- 1529 Reul N, Saux-Picart S, Chapron B, Vandemark D, Tournadre J, Salisbury J (2009),
1530 Demonstration of ocean surface salinity microwave measurements from space
1531 using AMSR-E over the Amazon plume, *Geophys. Res. Letters*, 36, L13607
- 1532 Reul, N, Tenerelli J (2011) SMOS Level 3 SSS Research products - Product Validation
1533 Document - Reprocessed Year 2010. CECOS/CNES/IFREMER/CATDS Techn
1534 Doc (available from www.catds.fr).
- 1535 Reul N, Tenerelli J, Boutin J, Chapron B, Paul F, Brion E, Gaillard F, Archer O (2012)
1536 Overview of the First SMOS Sea Surface Salinity Products. Part I: Quality

- 1537 Assessment for the Second Half of 2010. *IEEE Transactions on Geoscience and*
1538 *Remote Sensing* 50 (5) : 1636 - 1647
- 1539 Reverdin G, Kestenare E, Frankignoul C, Delcroix T (2007), Sea surface salinity in the
1540 Atlantic Ocean (30°S–50°N), *Prog. Oceanogr.*, 73: 311–340
- 1541 Reverdin G, Morisset S, Boutin J, Martin N (2012) Rain-induced variability of near sea-
1542 surface *T* and *S* from drifter data, *J. Geophys. Res.*, 117, C02032
- 1543 Richardson PL, McKee T (1984) Average seasonal variation of the atlantic equatorial
1544 currents from historical ship drifts, *Journal of Physical Oceanography*,
1545 14(7):1226-1238
- 1546 Ruf CS, Swift CT, Tanner AB, Le Vine DM(1988)Interferometric synthetic aperture
1547 microwave radiometry for the remote sensing of the Earth.*IEEE Transactions on*
1548 *Geoscience and Remote Sensing*, 26, pp. 597-611.
- 1549 Salisbury J, Vandemark D, Campbell J, Hunt C, Wisser D, Reul N, Chapron B (2011)
1550 Spatial and temporal coherence between Amazon River discharge, salinity, and
1551 light absorption by colored organic carbon in western tropical Atlantic surface
1552 waters, *J. Geophys. Res.*, 116, C00H02
- 1553 Schlössel P, Soloviev A, Emery WJ (1997) Cool and freshwater skin of the ocean during
1554 rainfall, *Boundary-Layer Meteorology* 82 (3): 439-474
- 1555 Schmitt RW(2008) Salinity and the global water cycle, *Oceanography* 21(1):12–19
- 1556 Singh A, Delcroix T, Cravatte S (2011) Contrasting the flavors of El Niño-Southern
1557 Oscillation using sea surface salinity observations, *J. Geophys. Res.*, 116: C06016
- 1558 Smith WO, Demaster DJ (1996) Phytoplankton biomass and productivity in the amazon
1559 river plume: correlation with seasonal river discharge, *Continental Shelf*
1560 *Research*, 16(3):291-319
- 1561 Soloviev A, Lukas R (1996) Observation of spatial variability of diurnal thermocline and
1562 rainformed halocline in the Western Pacific warm pool, *J. Phys. Oceanogr.*, 26:
1563 2529– 2538
- 1564 Steven DM, Brooks AL (1972), Identification of amazon river water at barbados, w. indies,
1565 by salinity and silicate measurements, *Marine Biology*, 14(4): 345-348
- 1566 Ternon, JF, Oudot C, Dessier A, Diverres D (2000) A seasonal tropical sink for
1567 atmospheric CO₂ in the atlantic ocean: the role of the amazon river discharge,
1568 *Marine Chemistry* 68(3): 183-201
- 1569 Terray L, Corre L, Cravatte S, Delcroix T, Reverdin G, Ribes A. (2011) Near-surface
1570 salinity as nature's rain gauge to detect human influence on the tropical water cycle,
1571 *J. Climate*, 25:958–977
- 1572 Twardowski MS, Donaghay PL (2001) Separating in situ and terrigenous sources of
1573 absorption by dissolved material in coastal waters, *J. Geophys. Res.*, 106(C2):
1574 2545– 2560

- 1575 UNESCO: The international system of units (SI) in oceanography, UNESCO Technical
1576 Papers No. 45, IAPSO Pub. Sci. No. 32, Paris, France, 1985.
- 1577 Van Bennekom AJ, Jager JE (1978) Dissolved aluminium in the Zaire river plume, Neth.
1578 J. Sea Res. 12 (3/4): 358-367.
- 1579 Van Bennekom AJ, Berger GW (1984), Hydrography and silica Budget of the Angola
1580 Basin, Netherlands Journal of Sea Research 17 (2-4): 149-200
- 1581 Vangriesheim A, Pierre C, Aminot A, Metzl N, Baurand F, Caprais JC (2009) The
1582 influence of Congo river discharges in the surface and deep layers of the gulf of
1583 guinea, Deep Sea Research Part II: Topical Studies in Oceanography 56(23):
1584 2183-2196
- 1585 Vialard J, Delecluse P (1998a) An OGCM Study for the TOGA Decade. Part I : Role of
1586 Salinity in the Physics of the Western Pacific Fresh Pool. Journal of Physical
1587 Oceanography, 28: 1071 - 1088
- 1588 Vialard J, Delecluse P (1998b) An OGCM Study for the TOGA Decade. Part II : Barrier
1589 Layer Formation and Variability. Journal of Physical Oceanography, 28:1089 -1106
- 1590 Vizy EK, Cook KH (2010) Influence of the Amazon/Orinoco Plume on the summertime
1591 Atlantic climate, J. Geophys. Res., 115, D21112
- 1592 Vörösmarty CJ, Fekete B, Tucker BA (1998) River discharge Database, Version 1.1
1593 (RivDIS v1.0 supplement). Institute for the Study of Earth, Oceans, and Space,
1594 University of New Hampshire, Durham, NH
- 1595 Wang X, Han G, Qi, Y, Li W (2011) Impact of barrier layer on typhoon-induced sea
1596 surface cooling, Dynamics of Atmospheres and Oceans, 52, 3: 367-385
- 1597 Wauthy B (1977) - Révision de la classification des eaux de surface du golfe de Guinée.
1598 Cah. O.R.S.T.O.M., sér. Océanogr., 15 (3) : 279-295.
- 1599 Wijesekera HW, Paulson CA, Huyer A (1999) The effect of rainfall on the surface layer
1600 during a westerly wind burst in the western equatorial Pacific, J. Phys. Oceanogr.,
1601 29: 612– 632
- 1602 Wisser D, Fekete BM, Vörösmarty CJ, Schumann AH (2010) Reconstructing 20th century
1603 global hydrography: A contribution to the Global Terrestrial Network-Hydrology
1604 (GTN-H), Hydrol. Earth Syst. Sci., 14: 1–24
- 1605 Yamashita Y, Tanoue E (2004), In situ production of chromophoric dissolved organic
1606 matter in coastal environments, Geophys. Res. Lett. 31: L14302
- 1607 Yin X, Boutin J, Martin N, Spurgeon P (2012) Optimization of L-Band Sea Surface
1608 Emissivity Models Deduced From SMOS Data, IEEE Transactions on Geoscience
1609 and Remote Sensing 50: 1414-1426
- 1610 Yoo JM, Carton JA (1988), Spatial Dependence of the Relationship between Rainfall and
1611 Outgoing Longwave Radiation in the Tropical Atlantic., Journal of Climate, 1:
1612 1047- 1056

- 1613 Yu L, Weller RA (2007) Objectively Analyzed air-sea heat Fluxes (OAFlux) for the global
1614 ocean, Bull. Am. Meteorol. Soc., 88(4): 527–539
- 1615 Yu L (2010) On Sea Surface Salinity Skin Effect Induced by Evaporation and Implications
1616 for Remote Sensing of Ocean Salinity, Journal of Physical Oceanography 40 (1) 85
- 1617 Yu L (2011) A global relationship between the ocean water cycle and near-surface
1618 salinity, Journal of geophysical Research, 116: C10025
- 1619 Yu L, McPhaden MJ (2011) Ocean pre-conditioning of Cyclone Nargis in the Bay of
1620 Bengal: Interaction between Rossby waves, surface fresh waters, and sea surface
1621 temperatures. J. Phys. Oceanogr., 41, 1741-1755.
- 1622 Yueh SH, West R, Wilson WJ, Li FK, Njoku EG, Rahmatsamii Y (2001), Error sources
1623 and feasibility for microwave remote sensing of ocean surface salinity. IEEE
1624 Transactionson Geoscience and Remote Sensing, 39: 1049-1060
- 1625 Zhang Y, Zhang X (2012) Ocean haline skin layer and turbulent surface convections, J.
1626 Geophys. Res., 117, C04017
- 1627
- 1628